
Going Beyond Linear Mode Connectivity: The Layerwise Linear Feature Connectivity

Zhanpeng Zhou¹, Yongyi Yang², Xiaojiang Yang¹, Junchi Yan^{1*}, Wei Hu²

¹Shanghai Jiao Tong University, ² University of Michigan

{zzp1012, yangxiaojiang, yanjunchi}@sjtu.edu.cn,
{tyongyi, vvh}@umich.edu

Abstract

Recent work has revealed many intriguing empirical phenomena in neural network training, despite the poorly understood and highly complex loss landscapes and training dynamics. One of these phenomena, Linear Mode Connectivity (LMC), has gained considerable attention due to the intriguing observation that different solutions can be connected by a linear path in the parameter space while maintaining near-constant training and test losses. In this work, we introduce a stronger notion of linear connectivity, *Layerwise Linear Feature Connectivity* (LLFC), which says that the feature maps of every layer in different trained networks are also linearly connected. We provide comprehensive empirical evidence for LLFC across a wide range of settings, demonstrating that whenever two trained networks satisfy LMC (via either spawning or permutation methods), they also satisfy LLFC in nearly all the layers. Furthermore, we delve deeper into the underlying factors contributing to LLFC, which reveal new insights into the spawning and permutation approaches. The study of LLFC transcends and advances our understanding of LMC by adopting a feature-learning perspective. Source code will be made publicly available.

1 Introduction

Despite the successes of modern deep neural networks, theoretical understanding of them still lags behind. Efforts to understand the mechanisms behind deep learning have led to significant interest in exploring the loss landscapes and training dynamics. While the loss functions used in deep learning are often regarded as complex black-box functions in high dimensions, it is believed that these functions, particularly the parts encountered in practical training trajectories, contain intricate benign structures that play a role in facilitating the effectiveness of gradient-based training. Just like in many other scientific disciplines, a crucial step toward formulating a comprehensive theory of deep learning lies in meticulous empirical investigations of the learning pipeline, intending to uncover quantitative and reproducible nontrivial phenomena that shed light on the underlying mechanisms.

One intriguing phenomenon discovered in recent work is Mode Connectivity [9, 4, 10]: Different optima found by independent runs of gradient-based optimization are connected by a simple path in the parameter space, on which the loss or accuracy is nearly constant. This is surprising as different optima of a non-convex function can very well reside in different and isolated “valleys” and yet this does not happen for optima found in practice. More recently, an even stronger form of mode connectivity called Linear Mode Connectivity (LMC) was discovered [8]. It depicts that different optima can be connected by a *linear* path of constant loss/accuracy. Although LMC typically does not happen for two independently trained networks, it has been consistently observed in the following scenarios:

* Corresponding author.

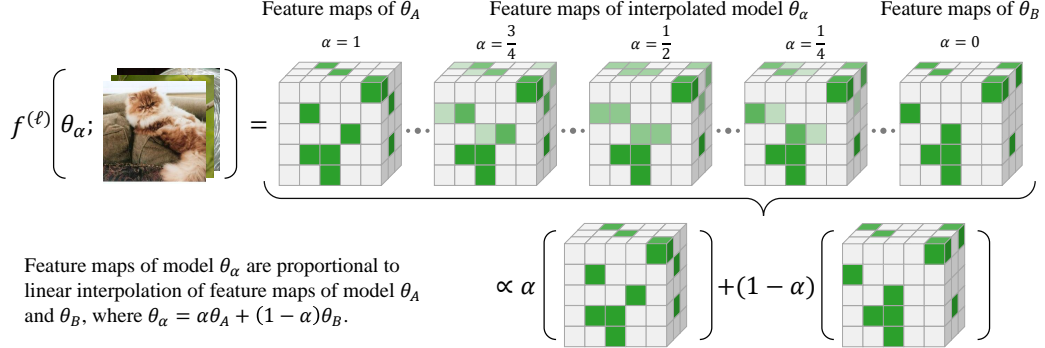


Figure 1: Illustration of Layerwise Linear Feature Connectivity (LLFC).

- **Spawning** [8]: A network is randomly initialized, trained for a small number of epochs (e.g. 5 epochs for both ResNet-20 and VGG-16 on the CIFAR-10 dataset), and then spawned into two copies which continue to be independently trained using different SGD randomnesses (i.e., for mini-batch order and data augmentation).

- **Permutation** [5, 1]: Two networks are independently trained, and the weights of one of them are allowed to be permuted while maintaining a functionally equivalent network.

The study of LMC is highly motivated due to its ability to unveil nontrivial structural properties of loss landscapes and training dynamics. Furthermore, LMC has significant relevance to various practical applications, such as pruning and weight-averaging methods.

On the other hand, the success of deep neural networks is related to their ability to learn useful *features*, or *representations*, of the data [24], and recent work has highlighted the importance of analyzing not only the final outputs of a network but also its intermediate features [18]. However, this crucial perspective is absent in the existing literature on LMC and weight averaging. These studies typically focus on interpolating the weights of different models and examining the final loss and accuracy, without delving into the internal layers of the network.

In this work, we take a feature-learning perspective on LMC and pose the question: what happens to the internal features when we linearly interpolate the weights of two trained networks? Our main discovery, referred to as *Layerwise Linear Feature Connectivity (LLFC)*, is that the features in almost all the layers also satisfy a strong form of linear connectivity: the feature map in the weight-interpolated network is approximately the same as the linear interpolation of the feature maps in the two original networks. More precisely, let θ_A and θ_B be the weights of two trained networks, and let $f^{(\ell)}(\theta)$ be the feature map in the ℓ -th layer of the network with weights θ . Then we say that θ_A and θ_B satisfy LLFC if

$$f^{(\ell)}(\alpha\theta_A + (1 - \alpha)\theta_B) \propto \alpha f^{(\ell)}(\theta_A) + (1 - \alpha)f^{(\ell)}(\theta_B), \quad \forall \alpha \in [0, 1], \forall \ell. \quad (1)$$

See Figure 1 for an illustration. While LLFC certainly cannot hold for two arbitrary θ_A and θ_B , we find that it is satisfied whenever θ_A and θ_B satisfy LMC. We confirm this across a wide range of settings, as well as for both spawning and permutation methods that give rise to LMC.

LLFC is a much finer-grained characterization of linearity than LMC. While LMC only concerns loss or accuracy, which is a single scalar value, LLFC (1) establishes a relation for all intermediate feature maps, which are high-dimensional objects. Furthermore, it is not difficult to see that LLFC applied to the output layer implies LMC when the two networks have small errors (see Lemma 1); hence, LLFC can be viewed as a strictly stronger property than LMC. The consistent co-occurrence of LLFC and LMC suggests that studying LLFC may play a crucial role in enhancing our understanding of LMC.

Subsequently, we delve deeper into the underlying factors contributing to LLFC. We identify two critical conditions, *weak additivity for ReLU function* and a *commutativity property* between two trained networks. We prove that these two conditions collectively imply LLFC in ReLU networks, and provide empirical verification of these conditions. Furthermore, our investigation yields novel insights into both spawning and permutation approaches:

- For spawning, we find that when two networks undergo joint training for a few epochs before being split, they share similar top principal directions in their weights in each layer, which gives rise to the commutativity property.
- For permutation, we interpret both the activation matching and weight matching objectives in Git Re-Basin [1] as ways to ensure the satisfaction of commutativity property.

In summary, our work unveils a richer set of phenomena that go significantly beyond the scope of LMC, and our further investigation provides valuable insights into the underlying mechanism behind LMC. Our results demonstrate the value of opening the black box of neural networks and taking a feature-centric viewpoint in studying questions related to loss landscapes and training dynamics.

2 Related Work

(Linear) Mode Connectivity. Freeman and Bruna [9], Draxler et al. [4], Garipov et al. [10] observed Mode Connectivity, i.e., different optima/modes of the loss function can be connected through a non-linear path with nearly constant loss. Nagarajan and Kolter [21] first observed Linear Mode Connectivity (LMC), i.e., the near-constant-loss connecting path can be linear, on models trained on MNIST starting from the same random initialization. Later, Frankle et al. [8] observed LMC on harder datasets, for networks that are jointly trained for a short amount of time before going through independent training (we refer to this as the spawning method). Frankle et al. [8] also demonstrated a connection between LMC and the Lottery Ticket Hypothesis [7]. Fort et al. [6] used the spawning method to explore the connection between LMC and the Neural Tangent Kernel dynamics. Yunis et al. [32] showed that LMC also extends beyond two optima and identified a high-dimensional convex hull of low loss between multiple optima. On the theory side, several papers [9, 19, 28, 23, 22, 15] were able to prove non-linear mode connectivity under various settings, but there has not been a theoretical explanation of LMC to our knowledge.

Permutation Invariance. Neural network architectures contain permutation symmetries [12]: one can permute the weights in different layers while not changing the function computed by the network. Ashmore and Gashler [2] utilized the permutation invariance of DNNs to align the topological structure of two neural networks. Tattro et al. [27] used permutation invariance to align the neurons of two neural networks, resulting in improved non-linear mode connectivity. In the context of LMC, Entezari et al. [5], Ainsworth et al. [1] showed that even independently trained networks can be linearly connected when permutation invariance is taken into account. In particular, Ainsworth et al. [1] approached the neuron alignment problem by formulating it as bipartite graph matching and proposed two matching methods: activation matching and weight matching. Notably, Ainsworth et al. [1] achieved the first demonstration of LMC between independently trained ResNet models on the CIFAR-10 dataset using weight matching.

Model Averaging Methods. LMC also has direct implications for model averaging methods, which are further related to federated learning and ensemble methods. Wang et al. [29] introduced a novel federated learning algorithm that incorporates unit permutation before model averaging. Singh and Jaggi [26], Liu et al. [20] approached the neuron alignment problem in model averaging by formulating it as an optimal transport and graph matching problem, respectively. Wortsman et al. [31] averaged the weights of multiple fine-tuned models trained with different hyper-parameters and obtained improved performance.

3 Background and Preliminaries

Notation and Setup. Denote $[k] = \{1, 2, \dots, k\}$. We consider a classification dataset $\mathcal{D} = \{(\mathbf{x}_i, y_i)\}_{i=1}^n$, where $\mathbf{x}_i \in \mathbb{R}^{d_0}$ represents the input and $y_i \in [c]$ represents the label of the i -th data point. Here, n is the dataset size, d_0 is the input dimension and c is the number of classes. Moreover, we use $\mathbf{X} \in \mathbb{R}^{d_0 \times n}$ to stack all the input data into a matrix.

We consider an L -layer neural network of the form $f(\boldsymbol{\theta}; \mathbf{x})$, where $\boldsymbol{\theta}$ represents the model parameters, \mathbf{x} is the input, and $f(\boldsymbol{\theta}; \mathbf{x}) \in \mathbb{R}^c$. Let the ℓ -th layer feature (post-activation) of the network be $f^{(\ell)}(\boldsymbol{\theta}; \mathbf{x}) \in \mathbb{R}^{d_\ell}$, where d_ℓ is the dimension of the ℓ -th layer ($0 \leq \ell \leq L$) and $d_L = c$. Note that $f^{(0)}(\boldsymbol{\theta}; \mathbf{x}) = \mathbf{x}$ and $f^{(L)}(\boldsymbol{\theta}; \mathbf{x}) = f(\boldsymbol{\theta}; \mathbf{x})$. For an input data matrix \mathbf{X} , we also use $f(\boldsymbol{\theta}; \mathbf{X}) \in \mathbb{R}^{c \times n}$ and $f^{(\ell)}(\boldsymbol{\theta}; \mathbf{X}) \in \mathbb{R}^{d_\ell \times n}$ to denote the collection of the network outputs and features on all the datapoints, respectively. When \mathbf{X} is clear from the context, we simply write $f^{(\ell)}(\boldsymbol{\theta}) = f^{(\ell)}(\boldsymbol{\theta}; \mathbf{X})$ and $f(\boldsymbol{\theta}) = f(\boldsymbol{\theta}; \mathbf{X})$. Unless otherwise specified, in this paper we consider models trained on a training set, and then all the investigations are evaluated on a test set.

We use $\text{Err}_{\mathcal{D}}(\boldsymbol{\theta})$ to denote the classification error of the network $f(\boldsymbol{\theta}; \cdot)$ on the dataset \mathcal{D} .

Linear Mode Connectivity (LMC). We recall the notion of LMC in Definition 1.

Definition 1 (Linear Mode Connectivity). *Given a test dataset \mathcal{D} and two modes² $\boldsymbol{\theta}_A$ and $\boldsymbol{\theta}_B$ such that $\text{Err}_{\mathcal{D}}(\boldsymbol{\theta}_A) \approx \text{Err}_{\mathcal{D}}(\boldsymbol{\theta}_B)$, we say $\boldsymbol{\theta}_A$ and $\boldsymbol{\theta}_B$ are linearly connected if they satisfy*

$$\text{Err}_{\mathcal{D}}(\alpha\boldsymbol{\theta}_A + (1 - \alpha)\boldsymbol{\theta}_B) \approx \text{Err}_{\mathcal{D}}(\boldsymbol{\theta}_A), \quad \forall \alpha \in [0, 1]. \quad (2)$$

As Definition 1 shows, $\boldsymbol{\theta}_A$ and $\boldsymbol{\theta}_B$ satisfy LMC if the error metric on the linear path connecting their weights is nearly constant. There are two known methods to obtain linearly connected modes, the *spawning method* [8, 6] and the *permutation method* [5, 1].

Spawning Method. We start from random initialization $\boldsymbol{\theta}^{(0)}$ and train the model for k steps to obtain $\boldsymbol{\theta}^{(k)}$. Then we create two copies of $\boldsymbol{\theta}^{(k)}$ and continue training the two models separately using independent SGD randomnesses (mini-batch order and data augmentations) until convergence. By selecting a proper value of k (usually a small fraction of the total training steps), we can obtain two linearly connected modes.

Permutation Method. Due to permutation symmetry, it is possible to permute the weights in a neural network appropriately while not changing the function being computed. Given two modes $\boldsymbol{\theta}_A$ and $\boldsymbol{\theta}_B$ which are independently trained (and not linearly connected), the permutation method aims to find a permutation π such that the permuted mode $\boldsymbol{\theta}'_B = \pi(\boldsymbol{\theta}_B)$ is functionally equivalent to $\boldsymbol{\theta}_B$ and that $\boldsymbol{\theta}'_B$ and $\boldsymbol{\theta}_A$ are linearly connected. In other words, even if two modes are not linearly connected in the parameter space, they might still be linearly connected if permutation invariance is taken into account.

Among existing permutation methods, Git Re-Basin [1] is a representative one, which was the first to successfully achieve linear connectivity between two independently trained ResNet models on CIFAR-10. Specifically, a permutation π that maintains functionally equivalent network can be formulated by a set of per-layer permutations $\pi = \{\mathbf{P}^{(\ell)}\}_{\ell=1}^{L-1}$ where $\mathbf{P}^{(\ell)} \in \mathbb{R}^{d_\ell \times d_\ell}$ is a permutation matrix. Ainsworth et al. [1] proposed two distinct matching objectives for aligning the neurons of independently trained models via permutation: *weight matching* and *activation matching*:

$$\text{Weight matching: } \min_{\pi} \|\boldsymbol{\theta}_A - \pi(\boldsymbol{\theta}_B)\|^2. \quad (3)$$

$$\text{Activation matching: } \min_{\pi} \sum_{\ell=1}^{L-1} \|\mathbf{H}_A^{(\ell)} - \mathbf{P}^{(\ell)} \mathbf{H}_B^{(\ell)}\|_F^2. \quad (4)$$

Here, $\mathbf{H}_A^{(\ell)} = f^{(\ell)}(\boldsymbol{\theta}_A; \mathbf{X})$ is the ℓ -th layer feature matrix, and $\mathbf{H}_B^{(\ell)}$ is defined similarly.

Main Experimental Setup. In this paper, we use both the spawning method and the permutation method to obtain linearly connected modes. Following Frankle et al. [8], Ainsworth et al. [1], we perform our experiments on commonly used image classification datasets MNIST [16] and CIFAR-10 [14], and with the standard network architectures ResNet-20 [11], VGG-16 [25], and MLP. We follow the same training procedures and hyper-parameters as in Frankle et al. [8], Ainsworth et al. [1]. Due to space limit, we defer some of the experimental results to the appendix. Notice that [1] increased the width of ResNet by 32 times in order to achieve zero barrier, and we also followed this setting in the experiments of the permutation method. The detailed settings and hyper-parameters are also described in Appendix D.1.

4 Layerwise Linear Feature Connectivity (LLFC)

In this section, we formally describe Layerwise Linear Feature Connectivity (LLFC) and provide empirical evidence of its consistent co-occurrence with LMC. We also show that LLFC applied to the last layer directly implies LMC.

Definition 2 (Layerwise Linear Feature Connectivity). *Given dataset \mathcal{D} and two modes $\boldsymbol{\theta}_A, \boldsymbol{\theta}_B$ of an L -layer neural network f , the modes $\boldsymbol{\theta}_A$ and $\boldsymbol{\theta}_B$ are said to be layerwise linearly feature connected if they satisfy*

$$\forall \ell \in [L], \forall \alpha \in [0, 1], \exists c > 0, \text{s.t. } c f^{(\ell)}(\alpha\boldsymbol{\theta}_A + (1 - \alpha)\boldsymbol{\theta}_B) = \alpha f^{(\ell)}(\boldsymbol{\theta}_A) + (1 - \alpha)f^{(\ell)}(\boldsymbol{\theta}_B). \quad (5)$$

²Following the terminology in literature, a *mode* refers to an optimal solution obtained at the end of training.

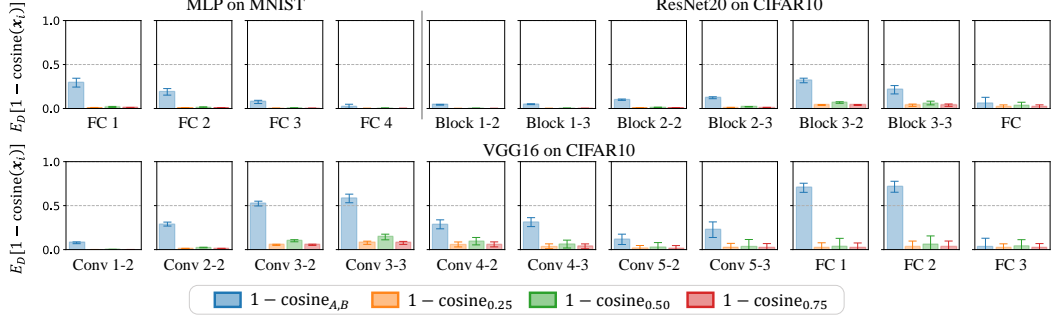


Figure 2: Comparison of $\mathbb{E}_{\mathcal{D}}[1 - \cosine_{\alpha}(\mathbf{x}_i)]$ and $\mathbb{E}_{\mathcal{D}}[1 - \cosine_{A,B}(\mathbf{x}_i)]$. The spawning method is used to obtain two linearly connected modes θ_A and θ_B . Results are presented for different layers of various model architectures on different datasets, with $\alpha \in \{0.25, 0.5, 0.75\}$. Standard deviations across the dataset are reported by error bars. More results are in Appendix D.2.

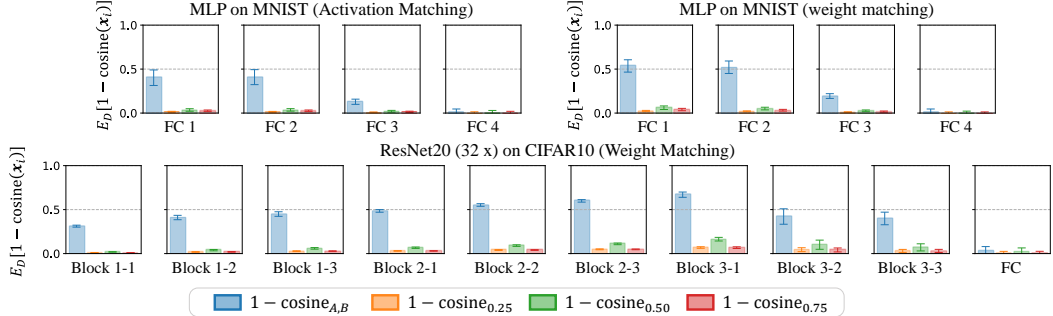


Figure 3: Comparison of $\mathbb{E}_{\mathcal{D}}[1 - \cosine_{\alpha}(\mathbf{x}_i)]$ and $\mathbb{E}_{\mathcal{D}}[1 - \cosine_{A,B}(\mathbf{x}_i)]$. The permutation method is used to obtain two linearly connected modes θ_A and θ_B . Results are presented for different layers of various model architectures on different datasets, with $\alpha \in \{0.25, 0.5, 0.75\}$. Standard deviations across the dataset are reported by error bars. More results are in Appendix D.2.

LLFC states that the per-layer feature of the interpolated model $\theta_{\alpha} = \alpha\theta_A + (1 - \alpha)\theta_B$ has the same direction as the linear interpolation of the features of θ_A and θ_B . This means that the feature map $f^{(\ell)}$ behaves similarly to a linear map (up to a scaling factor) on the line segment between θ_A and θ_B , even though it is a nonlinear map globally.

LLFC Co-occurs with LMC. We now verify that LLFC consistently co-occurs with LMC across different architectures and datasets. We use the spawning method and the permutation method described in Section 3 to obtain linearly connected modes θ_A and θ_B . On each data point \mathbf{x}_i in the test set \mathcal{D} , we measure the cosine similarity between the feature of the interpolated model θ_{α} and linear interpolations of the features of θ_A and θ_B in each layer ℓ , as expressed as $\cosine_{\alpha}(\mathbf{x}_i) = \cos[f^{(\ell)}(\alpha\theta_A + (1 - \alpha)\theta_B; \mathbf{x}_i), \alpha f^{(\ell)}(\theta_A; \mathbf{x}_i) + (1 - \alpha)f^{(\ell)}(\theta_B; \mathbf{x}_i)]$. We compare this to the baseline cosine similarity between the features of θ_A and θ_B in the corresponding layer, namely $\cosine_{A,B}(\mathbf{x}_i) = \cos[f^{(\ell)}(\theta_A; \mathbf{x}_i), f^{(\ell)}(\theta_B; \mathbf{x}_i)]$. The results for the spawning method and the permutation method are presented in Figures 2 and 3, respectively. They show that the values of $\mathbb{E}_{\mathcal{D}}[1 - \cosine_{\alpha}(\mathbf{x}_i)]$ are close to 0 across different layers, architectures, datasets, and different values of α , which verifies the LLFC property. The presence of small error bars indicates consistent behavior for each data point. Moreover, the values of $\mathbb{E}_{\mathcal{D}}[1 - \cosine_{A,B}(\mathbf{x}_i)]$ are not close to 0, which rules out the trivial case that $f^{(\ell)}(\theta_A)$ and $f^{(\ell)}(\theta_B)$ are already perfectly aligned.

LLFC Implies LMC. Intuitively, LLFC is a much stronger characterization than LMC since it establishes a linearity property in the high-dimensional feature map in every layer, rather than just for the final error. Lemma 1 below formally establishes that LMC is a consequence of LLFC by applying LLFC on the output layer.

Lemma 1 (Proof in Appendix A). *Suppose two modes θ_A, θ_B satisfy LLFC on a dataset \mathcal{D} and $\max\{\text{Err}_{\mathcal{D}}(\theta_A), \text{Err}_{\mathcal{D}}(\theta_B)\} \leq \epsilon$, then we have*

$$\forall \alpha \in [0, 1], \text{Err}_{\mathcal{D}}(\alpha\theta_A + (1 - \alpha)\theta_B) \leq 2\epsilon. \quad (6)$$

In summary, we see that the LMC property, which was used to study the loss landscapes in the entire parameter space, extends to the internal features in almost all the layers. LLFC offers much richer structural properties than LMC. In Section 5, we will dig deeper into the contributing factors to LLFC and leverage the insights to gain new understanding of the spawning and the permutation methods.

5 Why Does LLFC Emerge?

We have seen that LLFC is a prevalent phenomenon that co-occurs with LMC, and it establishes a broader notion of linear connectivity than LMC. In this section, we investigate the root cause of LLFC, and identify two key conditions, *weak additivity for ReLU activations* and *commutativity*. We verify these conditions empirically and prove that they collectively imply LLFC. From there, we provide an explanation for the effectiveness of both the spawning method and the permutation method, offering new insights into LMC.

5.1 Underlying Factors of LLFC

For convenience, we consider a multi-layer perceptron (MLP) in Section 5, though the results can be easily adapted to any feed-forward structure, e.g., a convolutional neural network³ (CNN). For an L -layer MLP f with ReLU activation, the weight matrix in the ℓ -th linear layer is denoted as $\mathbf{W}^{(\ell)} \in \mathbb{R}^{d_\ell \times d_{\ell-1}}$, and $\mathbf{b}^{(\ell)} \in \mathbb{R}^{d_\ell}$ is the bias in that layer. For a given input data matrix $\mathbf{X} \in \mathbb{R}^{d_0 \times n}$, denote the feature (post-activation) in the ℓ -th layer as $\mathbf{H}^{(\ell)} = f^{(\ell)}(\theta; \mathbf{X}) \in \mathbb{R}^{d_\ell \times n}$, and correspondingly pre-activation as $\tilde{\mathbf{H}}^{(\ell)} \in \mathbb{R}^{d_\ell \times n}$. The forward propagation in the ℓ -th layer is:

$$\mathbf{H}^{(\ell)} = \sigma(\tilde{\mathbf{H}}^{(\ell)}), \quad \tilde{\mathbf{H}}^{(\ell)} = \mathbf{W}^{(\ell)} \mathbf{H}^{(\ell-1)} + \mathbf{b}^{(\ell)} \mathbf{1}_{d_\ell}^\top.$$

Here, σ denotes the ReLU activation function, and $\mathbf{1}_{d_\ell} \in \mathbb{R}^{d_\ell}$ denotes the all-one vector. Additionally, we use $\mathbf{h}_i^{(\ell)}$ to denote the i -th row of $\mathbf{H}^{(\ell)}$, and $\tilde{\mathbf{h}}_i^{(\ell)}$ to denote the i -th row of $\tilde{\mathbf{H}}^{(\ell)}$, which correspond to the post- and pre-activations of the i -th input at layer ℓ , respectively.

Condition I: Weak Additivity for ReLU Activations.

Definition 3 (Weak Additivity for ReLU Activations). *Given a dataset \mathcal{D} , two modes θ_A and θ_B are said to satisfy weak additivity for ReLU activations if*

$$\forall \ell \in [L], \quad \sigma(\tilde{\mathbf{H}}_A^{(\ell)} + \tilde{\mathbf{H}}_B^{(\ell)}) = \sigma(\tilde{\mathbf{H}}_A^{(\ell)}) + \sigma(\tilde{\mathbf{H}}_B^{(\ell)}). \quad (7)$$

Definition 3 requires the ReLU activation function to behave like a linear function for the pre-activations in each layer of the two networks. Although this cannot be true in general since ReLU is a nonlinear function, we verify it empirically for modes that satisfy LMC and LLFC. Intuitively, weak additivity is related to the property that the pre-activations are *sparse*, meaning that for a given layer ℓ , most entries in the pre-activation $\tilde{\mathbf{H}}^{(\ell)}$ are close to zero. Note that if we consider $x, y \in \mathbb{R}$, where $|x| \leq \epsilon$ is small, we have $|\sigma(x + y) - \sigma(x) - \sigma(y)| \leq |x| \leq \epsilon$. Therefore, if most entries in $\tilde{\mathbf{H}}_A^{(\ell)}$ and $\tilde{\mathbf{H}}_B^{(\ell)}$ are small, Equation (7) is likely to approximately hold.

We conduct experiments on various datasets and architectures to validate weak additivity as well as the sparsity of $\tilde{\mathbf{H}}_A^{(\ell)}$ and $\tilde{\mathbf{H}}_B^{(\ell)}$. On each data point \mathbf{x}_i in the test set \mathcal{D} , we compute the normalized distance between the left-hand side and the right-hand side of Equation (7) for each layer ℓ . We denote the distance as $\text{Dist}_\sigma(\tilde{\mathbf{h}}_{i,A}, \tilde{\mathbf{h}}_{i,B}) = \text{dist}(\sigma(\tilde{\mathbf{h}}_{i,A} + \tilde{\mathbf{h}}_{i,B}), \sigma(\tilde{\mathbf{h}}_{i,A}) + \sigma(\tilde{\mathbf{h}}_{i,B}))$, where $\text{dist}(\mathbf{x}, \mathbf{y}) := \|\mathbf{x} - \mathbf{y}\|^2 / (\|\mathbf{x}\| \cdot \|\mathbf{y}\|)$. Additionally, we compare $\text{Dist}_\sigma(\tilde{\mathbf{h}}_{i,A}, \tilde{\mathbf{h}}_{i,B})$ with $\text{Dist}_\sigma(\mathbf{r}_1, \mathbf{r}_2)$,

³We also conduct experiments on CNNs. For a Conv layer, the forward propagation will be denoted as \mathbf{WH} similar to a linear layer. Typically, the weight \mathbf{W} for a Conv layer has shape (# of output channels, # of input channels, height, width) and we reshape \mathbf{W} to a matrix with dimensions (# of output channels, # of input channels \times height \times width).

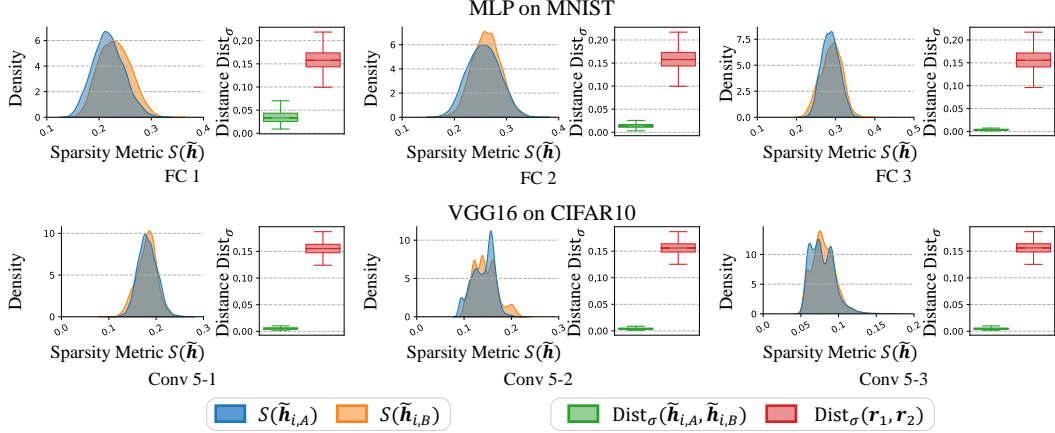


Figure 4: Distribution of the sparsity metrics $S(\tilde{h}_{i,A})$, $S(\tilde{h}_{i,B})$ over the test set and comparison between the distribution of the normalized distance $\text{Dist}_\sigma(\tilde{h}_{i,A}, \tilde{h}_{i,B})$ and $\text{Dist}_\sigma(r_1, r_2)$. The spawning method is used to obtain two modes that satisfy LLFC, θ_A and θ_B . Results are presented for different layers of MLP on MNIST and VGG-16 on CIFAR-10. Results of permutation methods are in Appendix D.3.

where r_1 and r_2 are independent d_ℓ -dimensional random vectors sampled from $\mathcal{N}(\mathbf{0}, \mathbf{I})$. Furthermore, to verify the sparsity of pre-activations, we measure $S(\mathbf{x}) = \frac{\|\mathbf{x}\|_1}{n\|\mathbf{x}\|_\infty}$ ($\mathbf{x} \in \mathbb{R}^n$) (The average absolute value of each entry in the vector dividing by the maximum absolute value among the entries). We measure the sparsity of the pre-activations of θ_A and θ_B in each layer over the dataset \mathcal{D} using this metric, denoted as $S(\tilde{h}_{i,A})$ and $S(\tilde{h}_{i,B})$, respectively. In Figure 4, we observe that across different datasets and model architectures, at different layers, the majority of $S(\tilde{h}_{i,A})$ and $S(\tilde{h}_{i,B})$ are small, thereby verifying the sparsity claim. More importantly, the normalized distances $\text{Dist}_\sigma(\tilde{h}_{i,A}, \tilde{h}_{i,B})$ are close to zero (and much smaller than the baseline $\text{Dist}_\sigma(r_1, r_2)$), which verifies the weak additivity condition.

Condition II: Commutativity.

Definition 4 (Commutativity). *Given a dataset \mathcal{D} , two modes θ_A and θ_B are said to satisfy commutativity if*

$$\forall \ell \in [L], \mathbf{W}_A^{(\ell)} \mathbf{H}_A^{(\ell-1)} + \mathbf{W}_B^{(\ell)} \mathbf{H}_B^{(\ell-1)} = \mathbf{W}_A^{(\ell)} \mathbf{H}_B^{(\ell-1)} + \mathbf{W}_B^{(\ell)} \mathbf{H}_A^{(\ell-1)}. \quad (8)$$

Commutativity depicts that the next-layer linear transformations applied to the internal features of two neural networks can be interchanged. This property is crucial for improving our understanding of LMC and LLFC. In Sections 5.2 and 5.3, we will use the commutativity property to provide new insights into both the spawning method and the permutation method.

We conduct experiments on various datasets and model architectures to verify the commutativity property for modes that satisfy LLFC. Specifically, for a given dataset \mathcal{D} and two modes θ_A and θ_B that satisfy LLFC, we compute the normalized distance between the left-hand side and the right-hand side of Equation (8), denoted as $\text{Dist}_{\text{com}} = \text{dist}(\text{vec}(\mathbf{W}_A^{(\ell)} \mathbf{H}_A^{(\ell-1)} + \mathbf{W}_B^{(\ell)} \mathbf{H}_B^{(\ell-1)}), \text{vec}(\mathbf{W}_A^{(\ell)} \mathbf{H}_B^{(\ell-1)} + \mathbf{W}_B^{(\ell)} \mathbf{H}_A^{(\ell-1)}))$. Furthermore, we compare Dist_{com} with the normalized distance between the weight matrices of the current layer ℓ , denoted as Dist_W , and the normalized distances between the post-activations of the previous layer $\ell - 1$, denoted as Dist_H . These distances are expressed as $\text{Dist}_W = \text{dist}(\text{vec}(\mathbf{W}_A^{(\ell)}), \text{vec}(\mathbf{W}_B^{(\ell)}))$ and $\text{Dist}_H = \text{dist}(\text{vec}(\mathbf{H}_A^{(\ell-1)}), \text{vec}(\mathbf{H}_B^{(\ell-1)}))$, respectively. Figure 5 shows that for both spawning and permutation methods, Dist_{com} is negligible compared with Dist_W and Dist_H , which confirms the commutativity condition. Note that we also rule out the trivial case where either the weight matrices or the post-activations in the two networks are already perfectly aligned, as weights and post-activations often differ significantly.

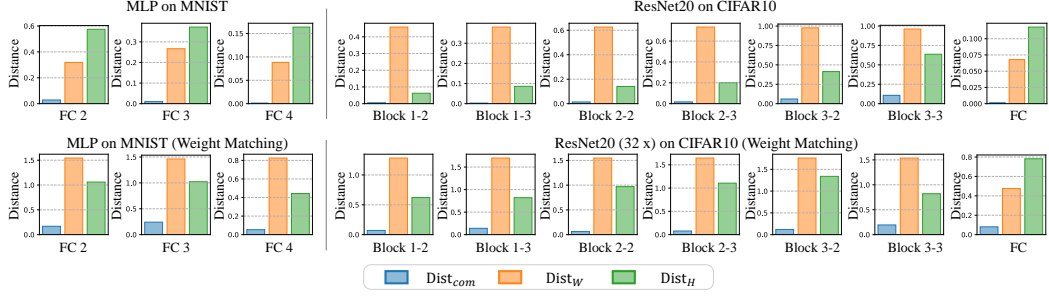


Figure 5: Comparison of Dist_{com} , Dist_W , and Dist_H . In the first row, the spawning method is used to acquire modes that satisfy LLFC, whereas the permutation method is used for the second row. For ResNet-20, Dist_{com} , Dist_W are calculated in the first Conv layer of each block. The results are presented for different layers of MLP on the MNIST and ResNet-20 on the CIFAR-10. More results are in Appendix D.4.

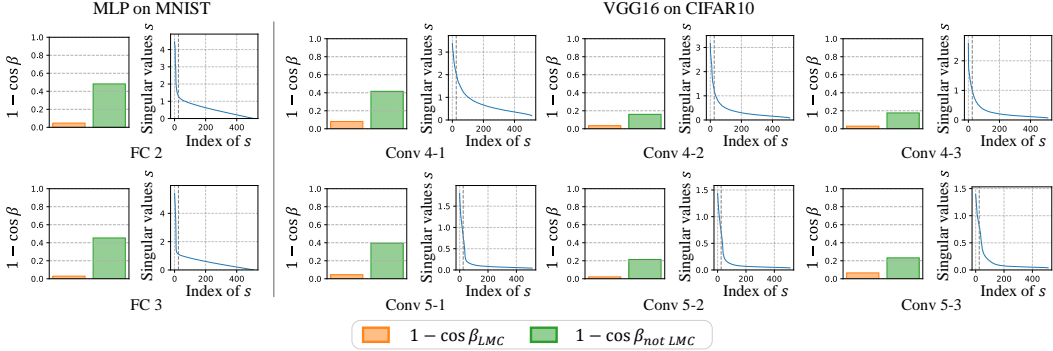


Figure 6: Comparison of $1 - \cos \beta_{LMC}$ and $1 - \cos \beta_{\text{not } LMC}$ and singular values of weight matrix of layers of θ_A in a descending order. The grey dashed line marked the value of k chosen for each β . The results are presented for different layers of MLP on the MNIST and ResNet-20 on the CIFAR-10. More results are in Appendix D.6.

Additionally, we note that commutativity has a similarity to model stitching [17, 3]. In Appendix D.5, we show that a stronger form of model stitching (without an additional trainable layer) works for two networks that satisfy LLFC.

Conditions I and II Imply LLFC. Theorem 1 below shows that weak additivity for ReLU activations (Definition 3) and commutativity (Definition 4) imply LLFC.

Theorem 1 (Proof in Appendix B). *Given a dataset \mathcal{D} , if two modes θ_A and θ_B satisfy weak additivity for ReLU activations (Definition 3) and commutativity (Definition 4), then*

$$\forall \alpha \in [0, 1], \forall \ell \in [L], f^{(\ell)}(\alpha \theta_A + (1 - \alpha) \theta_B) = \alpha f^{(\ell)}(\theta_A) + (1 - \alpha) f^{(\ell)}(\theta_B).$$

Note that the definition of LLFC (Definition 2) allows a scaling factor c , while Theorem 1 establishes a stronger version of LLFC where $c = 1$. We attribute this inconsistency to the accumulation of errors in weak additivity and commutativity conditions, since they are only approximated satisfied in practice. Yet in most cases, we observe that c is close to 1 (see Appendix D.2 for more results).

5.2 Insight into the Spawning Method

For the spawning method, while it is intuitively understood that the early phase of training plays a significant role in determining the fate of the final solution, it is not well understood why two spawned models would satisfy LMC if they undergo a small amount of common training at the beginning.

We discover that the modes found by the spawning method share similar principal directions of model weights in each layer, which in turn leads to the commutativity property (Definition 4). Specifically, when considering two modes θ_A and θ_B , we perform singular value decomposition to the weight

matrices of each layer ℓ as $\mathbf{W}_A^{(\ell)} = \mathbf{U}_A^{(\ell)} \boldsymbol{\Sigma}_A^{(\ell)} \mathbf{V}_A^{(\ell)\top}$ and $\mathbf{W}_B^{(\ell)} = \mathbf{U}_B^{(\ell)} \boldsymbol{\Sigma}_B^{(\ell)} \mathbf{V}_B^{(\ell)\top}$. We extract the first k columns from $\mathbf{U}_A^{(\ell)}$ and $\mathbf{U}_B^{(\ell)}$, which are singular vectors corresponding to the top- k singular values. Subsequently, we compute the minimal principal angle $\beta^{(\ell)}$ between the subspaces spanned by these extracted singular vectors of $\mathbf{U}_A^{(\ell)}$ and $\mathbf{U}_B^{(\ell)}$, respectively. In Figure 6, we compare the value of $1 - \cos \beta_{LMC}$ of two modes satisfying LMC to $1 - \cos \beta_{not\ LMC}$ of two modes that are independently trained (not satisfying LMC). Figure 6 shows that, across different datasets and model structures and for each layer, the angle β_{LMC} is close to zero while $\beta_{not\ LMC}$ is significantly larger, thereby verifying that the modes obtained by the spawning method share similar principal directions in their model weights.

The shared principal directions of model weights can lead to the satisfaction of the commutativity property, which we have shown to be critical for LLFC. Given two modes θ_A and θ_B obtained via spawning method, for each layer ℓ , we decompose the weight matrix $\mathbf{W}^{(\ell)}$ into the sum of two parts: the principle part $\mathbf{W}_{\text{pri}}^{(\ell)}$ and the negligible part $\mathbf{W}_{\text{neg}}^{(\ell)}$, and then we can obtain:

$$\begin{aligned} \mathbf{W}_A^{(\ell)} \mathbf{H}_A^{(\ell-1)} + \mathbf{W}_B^{(\ell)} \mathbf{H}_B^{(\ell-1)} &= (\mathbf{W}_{A,\text{pri}}^{(\ell)} + \mathbf{W}_{A,\text{neg}}^{(\ell)}) \mathbf{H}_A^{(\ell-1)} + (\mathbf{W}_{B,\text{pri}}^{(\ell)} + \mathbf{W}_{B,\text{neg}}^{(\ell)}) \mathbf{H}_B^{(\ell-1)} \\ &\approx \mathbf{W}_{A,\text{pri}}^{(\ell)} \mathbf{H}_A^{(\ell-1)} + \mathbf{W}_{B,\text{pri}}^{(\ell)} \mathbf{H}_B^{(\ell-1)} \\ &\stackrel{(i)}{\approx} \mathbf{W}_{B,\text{pri}}^{(\ell)} \mathbf{H}_A^{(\ell-1)} + \mathbf{W}_{B,\text{pri}}^{(\ell)} \mathbf{H}_A^{(\ell-1)} \\ &\approx \mathbf{W}_B^{(\ell)} \mathbf{H}_A^{(\ell-1)} + \mathbf{W}_A^{(\ell)} \mathbf{H}_B^{(\ell-1)}, \end{aligned}$$

where (i) is due to that $\mathbf{W}_A^{(\ell)}$ and $\mathbf{W}_B^{(\ell)}$ share similar principal parts. The above deduction implies that the commutativity property is naturally satisfied when two modes share similar principal directions in their model weights, thus leading to the satisfaction of LLFC.

5.3 Justification of the Permutation Methods

In this subsection, we provide a justification of the permutation methods in Git Re-Basin [1]: weight matching (3) and activation matching (4). Recall from Section 3 that given two modes θ_A and θ_B , the permutation method aims to find a permutation $\pi = \{\mathbf{P}^{(\ell)}\}_{\ell=1}^{L-1}$ such that the permuted $\theta'_B = \pi(\theta_B)$ and θ_A are linearly connected, where $\mathbf{P}^{(\ell)}$ is a permutation matrix applied to the ℓ -th layer feature. Concretely, with a permutation π , we can formulate $\mathbf{W}'_B^{(\ell)}$ and $\mathbf{H}'_B^{(\ell)}$ of θ'_B in each layer ℓ as $\mathbf{W}'_B^{(\ell)} = \mathbf{P}^{(\ell)} \mathbf{W}_B^{(\ell)} \mathbf{P}^{(\ell-1)\top}$ and $\mathbf{H}'_B^{(\ell)} = \mathbf{P}^{(\ell)} \mathbf{H}_B^{(\ell)}$ [1].⁴ In Section 5.1, we have identified the commutativity property as a key factor contributing to LLFC. The commutativity property (8) between θ_A and θ'_B can be written as

$$(\mathbf{W}_A^{(\ell)} - \mathbf{W}'_B^{(\ell)}) (\mathbf{H}_A^{(\ell-1)} - \mathbf{H}'_B^{(\ell-1)}) = \mathbf{0},$$

or

$$(\mathbf{W}_A^{(\ell)} - \mathbf{P}^{(\ell)} \mathbf{W}_B^{(\ell)} \mathbf{P}^{(\ell-1)\top}) (\mathbf{H}_A^{(\ell-1)} - \mathbf{P}^{(\ell-1)} \mathbf{H}_B^{(\ell-1)}) = \mathbf{0}. \quad (9)$$

We note that the weight matching (3) and activation matching (4) objectives can be written as $\min_{\pi} \sum_{\ell=1}^L \left\| \mathbf{W}_A^{(\ell)} - \mathbf{P}^{(\ell)} \mathbf{W}_B^{(\ell)} \mathbf{P}^{(\ell-1)\top} \right\|_F^2$ and $\min_{\pi} \sum_{\ell=1}^{L-1} \left\| \mathbf{H}_A^{(\ell)} - \mathbf{P}^{(\ell)} \mathbf{H}_B^{(\ell)} \right\|_F^2$, respectively, which directly correspond to the two factors in Equation (9). Therefore, we can interpret Git Re-Basin as a means to ensure commutativity. A more comprehensive analysis of Git Re-basin can be found in Appendix E.

6 Conclusion and Discussion

We identified Layerwise Linear Feature Connectivity (LLFC) as a prevalent phenomenon that co-occurs with Linear Mode Connectivity (LMC). By investigating the underlying contributing factors to LLFC, we obtained novel insights into the existing spawning and permutation methods that give rise to LMC. The consistent co-occurrence of LMC and LLFC suggests that LLFC may play an important role if we want to understand LMC in full. Since the LLFC phenomenon suggests that

⁴Note that both $\mathbf{P}^{(0)}$ and $\mathbf{P}^{(L)}$ are identity matrices.

averaging weights is roughly equivalent to averaging features, a natural future direction is to study feature averaging methods and investigate whether averaging leads to better features.

Finally, we leave the question if it is possible to find a permutation directly enforcing the commutativity property (9). Minimizing $\|(\mathbf{W}_A^{(\ell)} - \mathbf{P}^{(\ell)} \mathbf{W}_B^{(\ell)} \mathbf{P}^{(\ell-1)^\top})(\mathbf{H}_A^{(\ell-1)} - \mathbf{P}^{(\ell-1)} \mathbf{H}_B^{(\ell-1)})\|_F$ entails solving Quadratic Assignment Problems (QAPs) (See Appendix C for derivation), which are known NP-hard, calling for efficient techniques especially seeing the progress in learning to solve QAPs [30].

References

- [1] Samuel Ainsworth, Jonathan Hayase, and Siddhartha Srinivasa. Git re-basin: Merging models modulo permutation symmetries. In *The Eleventh International Conference on Learning Representations*, 2023. URL <https://openreview.net/forum?id=CQsmMYmlP5T>.
- [2] Stephen Ashmore and Michael Gashler. A method for finding similarity between multi-layer perceptrons by forward bipartite alignment. In *2015 International Joint Conference on Neural Networks (IJCNN)*, pages 1–7. IEEE, 2015.
- [3] Yamini Bansal, Preetum Nakkiran, and Boaz Barak. Revisiting model stitching to compare neural representations. In A. Beygelzimer, Y. Dauphin, P. Liang, and J. Wortman Vaughan, editors, *Advances in Neural Information Processing Systems*, 2021. URL <https://openreview.net/forum?id=ak06J5jNR4>.
- [4] Felix Draxler, Kambis Veschgini, Manfred Salmhofer, and Fred Hamprecht. Essentially no barriers in neural network energy landscape. In *International conference on machine learning*, pages 1309–1318. PMLR, 2018.
- [5] Rahim Entezari, Hanie Sedghi, Olga Saukh, and Behnam Neyshabur. The role of permutation invariance in linear mode connectivity of neural networks. In *International Conference on Learning Representations*, 2022. URL <https://openreview.net/forum?id=dNigytmkL>.
- [6] Stanislav Fort, Gintare Karolina Dziugaite, Mansheej Paul, Sepideh Kharaghani, Daniel M Roy, and Surya Ganguli. Deep learning versus kernel learning: an empirical study of loss landscape geometry and the time evolution of the neural tangent kernel. *Advances in Neural Information Processing Systems*, 33:5850–5861, 2020.
- [7] Jonathan Frankle and Michael Carbin. The lottery ticket hypothesis: Finding sparse, trainable neural networks. In *International Conference on Learning Representations*, 2019. URL <https://openreview.net/forum?id=rJ1-b3RcF7>.
- [8] Jonathan Frankle, Gintare Karolina Dziugaite, Daniel Roy, and Michael Carbin. Linear mode connectivity and the lottery ticket hypothesis. In *International Conference on Machine Learning*, pages 3259–3269. PMLR, 2020.
- [9] C. Daniel Freeman and Joan Bruna. Topology and geometry of half-rectified network optimization. In *International Conference on Learning Representations*, 2017. URL <https://openreview.net/forum?id=Bk0FWVcgx>.
- [10] Timur Garipov, Pavel Izmailov, Dmitrii Podoprikin, Dmitry P Vetrov, and Andrew G Wilson. Loss surfaces, mode connectivity, and fast ensembling of dnns. *Advances in neural information processing systems*, 31, 2018.
- [11] Kaiming He, Xiangyu Zhang, Shaoqing Ren, and Jian Sun. Deep residual learning for image recognition. In *2016 IEEE Conference on Computer Vision and Pattern Recognition (CVPR)*, pages 770–778, 2016. doi: 10.1109/CVPR.2016.90.
- [12] Robert Hecht-Nielsen. On the algebraic structure of feedforward network weight spaces. 1990.
- [13] Tjalling C Koopmans and Martin Beckmann. Assignment problems and the location of economic activities. *Econometrica: journal of the Econometric Society*, pages 53–76, 1957.
- [14] Alex Krizhevsky, Geoffrey Hinton, et al. Learning multiple layers of features from tiny images. 2009.
- [15] Rohith Kuditipudi, Xiang Wang, Holden Lee, Yi Zhang, Zhiyuan Li, Wei Hu, Rong Ge, and Sanjeev Arora. Explaining landscape connectivity of low-cost solutions for multilayer nets. *Advances in neural information processing systems*, 32, 2019.
- [16] Yann LeCun, Léon Bottou, Yoshua Bengio, and Patrick Haffner. Gradient-based learning applied to document recognition. *Proceedings of the IEEE*, 86(11):2278–2324, 1998.

[17] Karel Lenc and Andrea Vedaldi. Understanding image representations by measuring their equivariance and equivalence. In *Proceedings of the IEEE conference on computer vision and pattern recognition*, pages 991–999, 2015.

[18] Yixuan Li, Jason Yosinski, Jeff Clune, Hod Lipson, and John Hopcroft. Convergent learning: Do different neural networks learn the same representations? In Dmitry Storcheus, Afshin Rostamizadeh, and Sanjiv Kumar, editors, *Proceedings of the 1st International Workshop on Feature Extraction: Modern Questions and Challenges at NIPS 2015*, volume 44 of *Proceedings of Machine Learning Research*, pages 196–212, Montreal, Canada, 11 Dec 2015. PMLR. URL <https://proceedings.mlr.press/v44/li15convergent.html>.

[19] Shiyu Liang, Ruoyu Sun, Yixuan Li, and Rayadurgam Srikant. Understanding the loss surface of neural networks for binary classification. In *International Conference on Machine Learning*, pages 2835–2843. PMLR, 2018.

[20] Chang Liu, Chenfei Lou, Runzhong Wang, Alan Yuhan Xi, Li Shen, and Junchi Yan. Deep neural network fusion via graph matching with applications to model ensemble and federated learning. In *ICML*, pages 13857–13869, 2022. URL <https://proceedings.mlr.press/v162/liu22k.html>.

[21] Vaishnavh Nagarajan and J Zico Kolter. Uniform convergence may be unable to explain generalization in deep learning. *Advances in Neural Information Processing Systems*, 32, 2019.

[22] Quynh Nguyen. On connected sublevel sets in deep learning. In *International conference on machine learning*, pages 4790–4799. PMLR, 2019.

[23] Quynh Nguyen, Mahesh Chandra Mukkamala, and Matthias Hein. On the loss landscape of a class of deep neural networks with no bad local valleys. In *International Conference on Learning Representations*, 2019. URL <https://openreview.net/forum?id=HJgXsjA5tQ>.

[24] David E Rumelhart, Geoffrey E Hinton, and Ronald J Williams. Learning internal representations by error propagation. Technical report, California Univ San Diego La Jolla Inst for Cognitive Science, 1985.

[25] Karen Simonyan and Andrew Zisserman. Very deep convolutional networks for large-scale image recognition. In Yoshua Bengio and Yann LeCun, editors, *3rd International Conference on Learning Representations, ICLR 2015, San Diego, CA, USA, May 7-9, 2015, Conference Track Proceedings*, 2015. URL <http://arxiv.org/abs/1409.1556>.

[26] Sidak Pal Singh and Martin Jaggi. Model fusion via optimal transport. *Advances in Neural Information Processing Systems*, 33:22045–22055, 2020.

[27] Norman Tatro, Pin-Yu Chen, Payel Das, Igor Melnyk, Prasanna Sattigeri, and Rongjie Lai. Optimizing mode connectivity via neuron alignment. *Advances in Neural Information Processing Systems*, 33:15300–15311, 2020.

[28] Luca Venturi, Afonso S. Bandeira, and Joan Bruna. Spurious valleys in one-hidden-layer neural network optimization landscapes. *J. Mach. Learn. Res.*, 20:133:1–133:34, 2019. URL <http://jmlr.org/papers/v20/18-674.html>.

[29] Hongyi Wang, Mikhail Yurochkin, Yuekai Sun, Dimitris Papailiopoulos, and Yasaman Khazaeni. Federated learning with matched averaging. In *International Conference on Learning Representations*, 2020. URL <https://openreview.net/forum?id=BkluqlSFDS>.

[30] Runzhong Wang, Junchi Yan, and Xiaokang Yang. Neural graph matching network: Learning lawler’s quadratic assignment problem with extension to hypergraph and multiple-graph matching. *IEEE Transactions on Pattern Analysis and Machine Intelligence*, 2022.

[31] Mitchell Wortsman, Gabriel Ilharco, Samir Ya Gadre, Rebecca Roelofs, Raphael Gontijo-Lopes, Ari S Morcos, Hongseok Namkoong, Ali Farhadi, Yair Carmon, Simon Kornblith, et al. Model soups: averaging weights of multiple fine-tuned models improves accuracy without increasing inference time. In *International Conference on Machine Learning*, pages 23965–23998. PMLR, 2022.

[32] David Yunis, Kumar Kshitij Patel, Pedro Henrique Pamplona Savarese, Gal Vardi, Jonathan Frankle, Matthew Walter, Karen Livescu, and Michael Maire. On convexity and linear mode connectivity in neural networks. In *OPT 2022: Optimization for Machine Learning (NeurIPS 2022 Workshop)*, 2022. URL <https://openreview.net/forum?id=TZQ3PKL3fPr>.

A Proof of Lemma 1

In this section, we prove Lemma 1 in the main paper. This lemma indicates that we can directly imply Linear Mode Connectivity (LMC, see Definition 1) from Layerwise Linear Feature Connectivity (LLFC, see Definition 2) applied to last layer.

Definition 1 (Linear Mode Connectivity). *Given a test dataset \mathcal{D} and two modes θ_A and θ_B such that $\text{Err}_{\mathcal{D}}(\theta_A) \approx \text{Err}_{\mathcal{D}}(\theta_B)$, we say θ_A and θ_B are linearly connected if they satisfy*

$$\text{Err}_{\mathcal{D}}(\alpha\theta_A + (1 - \alpha)\theta_B) \approx \text{Err}_{\mathcal{D}}(\theta_A), \quad \forall \alpha \in [0, 1].$$

Definition 2 (Layerwise Linear Feature Connectivity). *Given dataset \mathcal{D} and two modes θ_A, θ_B of an L -layer neural network f , the modes θ_A and θ_B are said to be layerwise linearly feature connected if they satisfy*

$$\forall \ell \in [L], \forall \alpha \in [0, 1], \exists c > 0, \text{s.t. } cf^{(\ell)}(\alpha\theta_A + (1 - \alpha)\theta_B) = \alpha f^{(\ell)}(\theta_A) + (1 - \alpha) f^{(\ell)}(\theta_B).$$

Lemma 1. *Suppose two modes θ_A, θ_B satisfy LLFC on a dataset \mathcal{D} and*

$$\max \{\text{Err}_{\mathcal{D}}(\theta_A), \text{Err}_{\mathcal{D}}(\theta_B)\} \leq \epsilon,$$

then we have

$$\forall \alpha \in [0, 1], \text{Err}_{\mathcal{D}}(\alpha\theta_A + (1 - \alpha)\theta_B) \leq 2\epsilon.$$

Proof. Note that the classification depends on the relative order of the entries in the output of the final layer. As a consequence, for each data point in the dataset \mathcal{D} , the linear interpolation of the outputs of the models makes the correct classification if both models make the correct classification. Therefore, only if one of the model makes the incorrect classification, the linear interpolation of the outputs of the models would possibly make the incorrect classification, i.e,

$$\text{Err}_{\mathcal{D}}(\alpha f(\theta_A) + (1 - \alpha) f(\theta_B)) \leq \text{Err}_{\mathcal{D}}(\theta_A) + \text{Err}_{\mathcal{D}}(\theta_B).$$

Since θ_A and θ_B satisfy LLFC, then at last layer we have

$$f(\alpha\theta_A + (1 - \alpha)\theta_B) = \alpha f(\theta_A) + (1 - \alpha) f(\theta_B),$$

then have

$$\text{Err}_{\mathcal{D}}(\alpha\theta_A + (1 - \alpha)\theta_B) \leq \text{Err}_{\mathcal{D}}(\theta_A) + \text{Err}_{\mathcal{D}}(\theta_B).$$

According to the condition that

$$\max \{\text{Err}_{\mathcal{D}}(\theta_A), \text{Err}_{\mathcal{D}}(\theta_B)\} \leq \epsilon,$$

which indicates

$$\text{Err}_{\mathcal{D}}(\alpha\theta_A + (1 - \alpha)\theta_B) \leq 2\epsilon,$$

and this finishes the proof. \square

B Proof of Theorem 1

In this section, we prove Theorem 1 in the main paper. Theorem 1 indicates that we can derive LLFC from two simple conditions: weak additivity for ReLU activations (Definition 3) and commutativity (Definition 4). Note that though we consider a multi-layer perceptron (MLP) for convenience, our proof and results can be easily adopted to any feed-forward structure, e.g., a convolutional neural network (CNN).

Definition 3 (Weak Additivity for ReLU Activations). *Given a dataset \mathcal{D} , two modes θ_A and θ_B are said to satisfy weak additivity for ReLU activations if*

$$\forall \ell \in [L], \quad \sigma\left(\tilde{\mathbf{H}}_A^{(\ell)} + \tilde{\mathbf{H}}_B^{(\ell)}\right) = \sigma\left(\tilde{\mathbf{H}}_A^{(\ell)}\right) + \sigma\left(\tilde{\mathbf{H}}_B^{(\ell)}\right).$$

Definition 4 (Commutativity). *Given a dataset \mathcal{D} , two modes θ_A and θ_B are said to satisfy commutativity if*

$$\forall \ell \in [L], \mathbf{W}_A^{(\ell)} \mathbf{H}_A^{(\ell-1)} + \mathbf{W}_B^{(\ell)} \mathbf{H}_B^{(\ell-1)} = \mathbf{W}_A^{(\ell)} \mathbf{H}_B^{(\ell-1)} + \mathbf{W}_B^{(\ell)} \mathbf{H}_A^{(\ell-1)}.$$

Theorem 1. Given a dataset \mathcal{D} , if two modes $\boldsymbol{\theta}_A$ and $\boldsymbol{\theta}_B$ satisfy weak additivity for ReLU activations (Definition 3) and commutativity (Definition 4), then

$$\forall \alpha \in [0, 1], \forall \ell \in [L], f^{(\ell)}(\alpha \boldsymbol{\theta}_A + (1 - \alpha) \boldsymbol{\theta}_B) = \alpha f^{(\ell)}(\boldsymbol{\theta}_A) + (1 - \alpha) f^{(\ell)}(\boldsymbol{\theta}_B).$$

Proof. Before delving into the proof, let us denote the forward propagation in each layer ℓ by

$$\begin{aligned}\tilde{g}^{(\ell)}(\boldsymbol{\theta}; \mathbf{H}^{(\ell-1)}) &= \mathbf{W}^{(\ell)} \mathbf{H}^{(\ell-1)} + \mathbf{b}^{(\ell)} \mathbf{1}_{d_\ell}^\top \\ g^{(\ell)}(\boldsymbol{\theta}; \mathbf{H}^{(\ell-1)}) &= \sigma(\tilde{g}^{(\ell)}(\boldsymbol{\theta}; \mathbf{H}^{(\ell-1)})) = \mathbf{H}^{(\ell)}\end{aligned}$$

Given $\boldsymbol{\theta}_A$ and $\boldsymbol{\theta}_B$ that satisfy the commutativity property, then $\forall \ell \in [L]$ and $\forall \alpha \in [0, 1]$, we have

$$\begin{aligned}\mathbf{W}_A^{(\ell)} \mathbf{H}_A^{(\ell-1)} + \mathbf{W}_B^{(\ell)} \mathbf{H}_B^{(\ell-1)} &= \mathbf{W}_A^{(\ell)} \mathbf{H}_B^{(\ell-1)} + \mathbf{W}_B^{(\ell)} \mathbf{H}_A^{(\ell-1)} \\ \tilde{g}^{(\ell)}(\boldsymbol{\theta}_A; \mathbf{H}_A^{(\ell-1)}) + \tilde{g}^{(\ell)}(\boldsymbol{\theta}_B; \mathbf{H}_B^{(\ell-1)}) &= \tilde{g}^{(\ell)}(\boldsymbol{\theta}_A; \mathbf{H}_B^{(\ell-1)}) + \tilde{g}^{(\ell)}(\boldsymbol{\theta}_B; \mathbf{H}_A^{(\ell-1)}) \\ \alpha(1 - \alpha) \left(\tilde{g}^{(\ell)}(\boldsymbol{\theta}_A; \mathbf{H}_A^{(\ell-1)}) + \tilde{g}^{(\ell)}(\boldsymbol{\theta}_B; \mathbf{H}_B^{(\ell-1)}) \right) &= \alpha(1 - \alpha) \left(\tilde{g}^{(\ell)}(\boldsymbol{\theta}_A; \mathbf{H}_B^{(\ell-1)}) + \tilde{g}^{(\ell)}(\boldsymbol{\theta}_B; \mathbf{H}_A^{(\ell-1)}) \right) \\ \alpha \tilde{g}^{(\ell)}(\boldsymbol{\theta}_A; \mathbf{H}_A^{(\ell-1)}) + (1 - \alpha) \tilde{g}^{(\ell)}(\boldsymbol{\theta}_B; \mathbf{H}_B^{(\ell-1)}) &= \alpha^2 \tilde{g}^{(\ell)}(\boldsymbol{\theta}_A; \mathbf{H}_A^{(\ell-1)}) + (1 - \alpha)^2 \tilde{g}^{(\ell)}(\boldsymbol{\theta}_B; \mathbf{H}_B^{(\ell-1)}) \\ &\quad + \alpha(1 - \alpha) \left(\tilde{g}^{(\ell)}(\boldsymbol{\theta}_A; \mathbf{H}_B^{(\ell-1)}) + \tilde{g}^{(\ell)}(\boldsymbol{\theta}_B; \mathbf{H}_A^{(\ell-1)}) \right)\end{aligned}$$

Additionally, we can easily verify that

$$\begin{aligned}\tilde{g}^{(\ell)}(\alpha \boldsymbol{\theta}_A + (1 - \alpha) \boldsymbol{\theta}_B; \mathbf{H}^{(\ell)}) &= \alpha \tilde{g}^{(\ell)}(\boldsymbol{\theta}_A; \mathbf{H}^{(\ell)}) + (1 - \alpha) \tilde{g}^{(\ell)}(\boldsymbol{\theta}_B; \mathbf{H}^{(\ell)}) \\ \tilde{g}^{(\ell)}(\boldsymbol{\theta}; \alpha \mathbf{H}_A^{(\ell)} + (1 - \alpha) \mathbf{H}_B^{(\ell)}) &= \alpha \tilde{g}^{(\ell)}(\boldsymbol{\theta}; \mathbf{H}_A^{(\ell)}) + (1 - \alpha) \tilde{g}^{(\ell)}(\boldsymbol{\theta}; \mathbf{H}_B^{(\ell)})\end{aligned}$$

Subsequently,

$$\begin{aligned}\alpha \tilde{g}^{(\ell)}(\boldsymbol{\theta}_A; \mathbf{H}_A^{(\ell-1)}) + (1 - \alpha) \tilde{g}^{(\ell)}(\boldsymbol{\theta}_B; \mathbf{H}_B^{(\ell-1)}) &= \alpha \tilde{g}^{(\ell)}(\alpha \boldsymbol{\theta}_A + (1 - \alpha) \boldsymbol{\theta}_B; \mathbf{H}_A^{(\ell-1)}) \\ &\quad + (1 - \alpha) \tilde{g}^{(\ell)}(\alpha \boldsymbol{\theta}_A + (1 - \alpha) \boldsymbol{\theta}_B; \mathbf{H}_B^{(\ell-1)}) \\ &= \tilde{g}^{(\ell)}(\alpha \boldsymbol{\theta}_A + (1 - \alpha) \boldsymbol{\theta}_B; \alpha \mathbf{H}_A^{(\ell-1)} + (1 - \alpha) \mathbf{H}_B^{(\ell-1)}).\end{aligned}$$

Given the weak additivity for ReLU activation is satisfied for $\boldsymbol{\theta}_A$ and $\boldsymbol{\theta}_B$, then we have

$$\begin{aligned}\sigma(\alpha \tilde{g}^{(\ell)}(\boldsymbol{\theta}_A; \mathbf{H}_A^{(\ell-1)}) + (1 - \alpha) \tilde{g}^{(\ell)}(\boldsymbol{\theta}_B; \mathbf{H}_B^{(\ell-1)})) &= \sigma(\tilde{g}^{(\ell)}(\alpha \boldsymbol{\theta}_A + (1 - \alpha) \boldsymbol{\theta}_B; \alpha \mathbf{H}_A^{(\ell-1)} + (1 - \alpha) \mathbf{H}_B^{(\ell-1)})) \\ \alpha g^{(\ell)}(\boldsymbol{\theta}_A; \mathbf{H}_A^{(\ell-1)}) + (1 - \alpha) g^{(\ell)}(\boldsymbol{\theta}_B; \mathbf{H}_B^{(\ell-1)}) &= g^{(\ell)}(\alpha \boldsymbol{\theta}_A + (1 - \alpha) \boldsymbol{\theta}_B; \alpha \mathbf{H}_A^{(\ell-1)} + (1 - \alpha) \mathbf{H}_B^{(\ell-1)})\end{aligned}$$

To conclude, $\forall \ell \in [L]$ and $\forall \alpha \in [0, 1]$, we have

$$\alpha \mathbf{H}_A^{(\ell)} + (1 - \alpha) \mathbf{H}_B^{(\ell)} = g^{(\ell)}(\alpha \boldsymbol{\theta}_A + (1 - \alpha) \boldsymbol{\theta}_B; \alpha \mathbf{H}_A^{(\ell-1)} + (1 - \alpha) \mathbf{H}_B^{(\ell-1)}) \quad (10)$$

For the right hand side of Equation (10), recursively, we can have

$$\begin{aligned}g^{(\ell)}(\alpha \boldsymbol{\theta}_A + (1 - \alpha) \boldsymbol{\theta}_B; \alpha \mathbf{H}_A^{(\ell-1)} + (1 - \alpha) \mathbf{H}_B^{(\ell-1)}) &= g^{(\ell)}(\alpha \boldsymbol{\theta}_A + (1 - \alpha) \boldsymbol{\theta}_B; g^{(\ell-1)}(\alpha \boldsymbol{\theta}_A + (1 - \alpha) \boldsymbol{\theta}_B; \alpha \mathbf{H}_A^{(\ell-2)} + (1 - \alpha) \mathbf{H}_B^{(\ell-2)})) \\ &= (g^{(\ell)} \circ g^{(\ell-1)})(\alpha \boldsymbol{\theta}_A + (1 - \alpha) \boldsymbol{\theta}_B; \alpha \mathbf{H}_A^{(\ell-2)} + (1 - \alpha) \mathbf{H}_B^{(\ell-2)}) \\ &= \dots \\ &= (g^{(\ell)} \circ g^{(\ell-1)} \dots \circ g^{(1)})(\alpha \boldsymbol{\theta}_A + (1 - \alpha) \boldsymbol{\theta}_B; \mathbf{X}) \\ &= f^{(\ell)}(\alpha \boldsymbol{\theta}_A + (1 - \alpha) \boldsymbol{\theta}_B; \mathbf{X}),\end{aligned}$$

where \mathbf{X} denotes the input data matrix.

Recall we denote $\mathbf{H}^{(\ell)} = f^{(\ell)}(\boldsymbol{\theta}; \mathbf{X})$ which indicates

$$\alpha f^{(\ell)}(\boldsymbol{\theta}_A; \mathbf{X}) + (1 - \alpha) f^{(\ell)}(\boldsymbol{\theta}_B; \mathbf{X}) = f^{(\ell)}(\alpha \boldsymbol{\theta}_A + (1 - \alpha) \boldsymbol{\theta}_B; \mathbf{X}),$$

and this finishes the proof. \square

C Derivation of Quadratic Assignment Problem

In this section, we aim to show that minimizing $\sum_{\ell=1}^L \left\| \left(\mathbf{W}_A^{(\ell)} - \mathbf{P}^{(\ell)} \mathbf{W}_B^{(\ell)} \mathbf{P}^{(\ell-1)\top} \right) \left(\mathbf{H}_A^{(\ell-1)} - \mathbf{P}^{(\ell-1)} \mathbf{H}_B^{(\ell-1)} \right) \right\|_F^2$ includes solving Quadratic Assignment Problems (QAPs), known to be NP-hard.

$$\begin{aligned} & \arg \min_{\pi=\{\mathbf{P}^{(\ell)}\}} \sum_{\ell=1}^L \left\| \left(\mathbf{W}_A^{(\ell)} - \mathbf{P}^{(\ell)} \mathbf{W}_B^{(\ell)} \mathbf{P}^{(\ell-1)\top} \right) \left(\mathbf{H}_A^{(\ell-1)} - \mathbf{P}^{(\ell-1)} \mathbf{H}_B^{(\ell-1)} \right) \right\|_F^2 \\ \iff & \arg \min_{\pi=\{\mathbf{P}^{(\ell)}\}} \sum_{\ell=1}^L \left\| \mathbf{W}_A^{(\ell)} \mathbf{H}_A^{(\ell-1)} - \mathbf{P}^{(\ell)} \mathbf{W}_B^{(\ell)} \mathbf{P}^{(\ell-1)\top} \mathbf{H}_A^{(\ell-1)} - \mathbf{W}_A^{(\ell)} \mathbf{P}^{(\ell-1)} \mathbf{H}_B^{(\ell-1)} + \mathbf{P}^{(\ell)} \mathbf{W}_B^{(\ell)} \mathbf{H}_B^{(\ell-1)} \right\|_F^2 \\ \iff & \arg \min_{\pi=\{\mathbf{P}^{(\ell)}\}} \sum_{\ell=1}^L \left(\left\| \mathbf{W}_A^{(\ell)} \mathbf{H}_A^{(\ell-1)} - \mathbf{W}_A^{(\ell)} \mathbf{P}^{(\ell-1)} \mathbf{H}_B^{(\ell-1)} \right\|_F^2 + \left\| \mathbf{P}^{(\ell)} \mathbf{W}_B^{(\ell)} \mathbf{P}^{(\ell-1)\top} \mathbf{H}_A^{(\ell-1)} - \mathbf{P}^{(\ell)} \mathbf{W}_B^{(\ell)} \mathbf{H}_B^{(\ell-1)} \right\|_F^2 \right. \\ & \quad \left. + \left\langle \mathbf{W}_A^{(\ell)} \mathbf{H}_A^{(\ell-1)} - \mathbf{W}_A^{(\ell)} \mathbf{P}^{(\ell-1)} \mathbf{H}_B^{(\ell-1)}, \mathbf{P}^{(\ell)} \mathbf{W}_B^{(\ell)} \mathbf{P}^{(\ell-1)\top} \mathbf{H}_A^{(\ell-1)} - \mathbf{P}^{(\ell)} \mathbf{W}_B^{(\ell)} \mathbf{H}_B^{(\ell-1)} \right\rangle_F \right). \end{aligned}$$

Consider its first term, i.e.,

$$\begin{aligned} & \arg \min_{\pi=\{\mathbf{P}^{(\ell)}\}} \sum_{\ell=1}^L \left\| \mathbf{W}_A^{(\ell)} \mathbf{H}_A^{(\ell-1)} - \mathbf{W}_A^{(\ell)} \mathbf{P}^{(\ell-1)} \mathbf{H}_B^{(\ell-1)} \right\|_F^2 \\ \iff & \arg \min_{\pi=\{\mathbf{P}^{(\ell)}\}} \sum_{\ell=1}^L \text{tr} \left(\left(\mathbf{H}_A^{(\ell-1)\top} \mathbf{W}_A^{(\ell)\top} - \mathbf{H}_B^{(\ell-1)\top} \mathbf{P}^{(\ell-1)\top} \mathbf{W}_A^{(\ell)\top} \right) \left(\mathbf{W}_A^{(\ell)} \mathbf{H}_A^{(\ell-1)} - \mathbf{W}_A^{(\ell)} \mathbf{P}^{(\ell-1)} \mathbf{H}_B^{(\ell-1)} \right) \right) \\ \iff & \arg \min_{\pi=\{\mathbf{P}^{(\ell)}\}} \sum_{\ell=1}^L \text{tr} \left(\mathbf{H}_A^{(\ell-1)\top} \mathbf{W}_A^{(\ell)\top} \mathbf{W}_A^{(\ell)} \mathbf{H}_A^{(\ell-1)} - \mathbf{H}_B^{(\ell-1)\top} \mathbf{P}^{(\ell-1)\top} \mathbf{W}_A^{(\ell)\top} \mathbf{W}_A^{(\ell)} \mathbf{H}_A^{(\ell-1)} \right. \\ & \quad \left. - \mathbf{H}_A^{(\ell-1)\top} \mathbf{W}_A^{(\ell)\top} \mathbf{W}_A^{(\ell)} \mathbf{P}^{(\ell-1)} \mathbf{H}_B^{(\ell-1)} + \mathbf{H}_B^{(\ell-1)\top} \mathbf{P}^{(\ell-1)\top} \mathbf{W}_A^{(\ell)\top} \mathbf{W}_A^{(\ell)} \mathbf{P}^{(\ell-1)} \mathbf{H}_B^{(\ell-1)} \right) \\ \iff & \arg \min_{\pi=\{\mathbf{P}^{(\ell)}\}} \sum_{\ell=1}^L \text{tr} \left(-2 \mathbf{H}_B^{(\ell-1)\top} \mathbf{P}^{(\ell-1)\top} \mathbf{W}_A^{(\ell)\top} \mathbf{W}_A^{(\ell)} \mathbf{H}_A^{(\ell-1)} + \mathbf{H}_B^{(\ell-1)\top} \mathbf{P}^{(\ell-1)\top} \mathbf{W}_A^{(\ell)\top} \mathbf{W}_A^{(\ell)} \mathbf{P}^{(\ell-1)} \mathbf{H}_B^{(\ell-1)} \right) \\ \iff & \arg \min_{\pi=\{\mathbf{P}^{(\ell)}\}} \sum_{\ell=1}^L \text{tr} \left(-2 \mathbf{P}^{(\ell-1)\top} \mathbf{W}_A^{(\ell)\top} \mathbf{W}_A^{(\ell)} \mathbf{H}_A^{(\ell-1)} \mathbf{H}_B^{(\ell-1)\top} + \mathbf{P}^{(\ell-1)\top} \mathbf{W}_A^{(\ell)\top} \mathbf{W}_A^{(\ell)} \mathbf{P}^{(\ell-1)} \mathbf{H}_B^{(\ell-1)} \mathbf{H}_B^{(\ell-1)\top} \right) \\ \iff & \arg \min_{\pi=\{\mathbf{P}^{(\ell)}\}} \sum_{\ell=1}^L \left(\text{tr} \left(\mathbf{P}^{(\ell-1)\top} \mathbf{W}_A^{(\ell)\top} \mathbf{W}_A^{(\ell)} \mathbf{P}^{(\ell-1)} \mathbf{H}_B^{(\ell-1)} \mathbf{H}_B^{(\ell-1)\top} \right) - 2 \text{tr} \left(\mathbf{P}^{(\ell-1)\top} \mathbf{W}_A^{(\ell)\top} \mathbf{W}_A^{(\ell)} \mathbf{H}_A^{(\ell-1)} \mathbf{H}_B^{(\ell-1)\top} \right) \right) \end{aligned}$$

where $\text{tr} \left(\mathbf{P}^{(\ell-1)\top} \mathbf{W}_A^{(\ell)\top} \mathbf{W}_A^{(\ell)} \mathbf{P}^{(\ell-1)} \mathbf{H}_B^{(\ell-1)} \mathbf{H}_B^{(\ell-1)\top} \right) - 2 \text{tr} \left(\mathbf{P}^{(\ell-1)\top} \mathbf{W}_A^{(\ell)\top} \mathbf{W}_A^{(\ell)} \mathbf{H}_A^{(\ell-1)} \mathbf{H}_B^{(\ell-1)\top} \right)$

is in the form of Koopmans-Beckmann's QAP [13] for each $\mathbf{P}^{(\ell-1)}$ and known as NP-hard. Thus,

solving $\arg \min_{\pi=\{\mathbf{P}^{(\ell)}\}} \sum_{\ell=1}^L \left\| \mathbf{W}_A^{(\ell)} \mathbf{H}_A^{(\ell-1)} - \mathbf{W}_A^{(\ell)} \mathbf{P}^{(\ell-1)} \mathbf{H}_B^{(\ell-1)} \right\|_F^2$ is to solve $L - 1$ QAPs in parallel.

Similarly, consider the second term, i.e,

$$\begin{aligned}
& \arg \min_{\pi=\{\mathbf{P}^{(\ell)}\}} \sum_{\ell=1}^L \left\| \mathbf{P}^{(\ell)} \mathbf{W}_B^{(\ell)} \mathbf{P}^{(\ell-1)^\top} \mathbf{H}_A^{(\ell-1)} - \mathbf{P}^{(\ell)} \mathbf{W}_B^{(\ell)} \mathbf{H}_B^{(\ell-1)} \right\|_F^2 \\
& \iff \arg \min_{\pi=\{\mathbf{P}^{(\ell)}\}} \sum_{\ell=1}^L \left\| \mathbf{W}_B^{(\ell)} \mathbf{P}^{(\ell-1)^\top} \mathbf{H}_A^{(\ell-1)} - \mathbf{W}_B^{(\ell)} \mathbf{H}_B^{(\ell-1)} \right\|_F^2 \\
& \iff \arg \min_{\pi=\{\mathbf{P}^{(\ell)}\}} \sum_{\ell=1}^L \text{tr} \left(\left(\mathbf{H}_A^{(\ell-1)^\top} \mathbf{P}^{(\ell-1)^\top} \mathbf{W}_B^{(\ell)^\top} - \mathbf{H}_B^{(\ell-1)^\top} \mathbf{W}_B^{(\ell)^\top} \right) \left(\mathbf{W}_B^{(\ell)} \mathbf{P}^{(\ell-1)^\top} \mathbf{H}_A^{(\ell-1)} - \mathbf{W}_B^{(\ell)} \mathbf{H}_B^{(\ell-1)} \right) \right) \\
& \iff \arg \min_{\pi=\{\mathbf{P}^{(\ell)}\}} \sum_{\ell=1}^L \text{tr} \left(\mathbf{H}_A^{(\ell-1)^\top} \mathbf{P}^{(\ell-1)^\top} \mathbf{W}_B^{(\ell)^\top} \mathbf{W}_B^{(\ell-1)^\top} \mathbf{H}_A^{(\ell-1)} - \mathbf{H}_A^{(\ell-1)^\top} \mathbf{P}^{(\ell-1)^\top} \mathbf{W}_B^{(\ell)^\top} \mathbf{W}_B^{(\ell-1)^\top} \mathbf{H}_B^{(\ell-1)} \right. \\
& \quad \left. - \mathbf{H}_B^{(\ell-1)^\top} \mathbf{W}_B^{(\ell)^\top} \mathbf{W}_B^{(\ell-1)^\top} \mathbf{P}^{(\ell-1)^\top} \mathbf{H}_A^{(\ell-1)} + \mathbf{H}_B^{(\ell-1)^\top} \mathbf{W}_B^{(\ell)^\top} \mathbf{W}_B^{(\ell-1)^\top} \mathbf{H}_B^{(\ell-1)} \right) \\
& \iff \arg \min_{\pi=\{\mathbf{P}^{(\ell)}\}} \sum_{\ell=1}^L \text{tr} \left(\mathbf{H}_A^{(\ell-1)^\top} \mathbf{P}^{(\ell-1)^\top} \mathbf{W}_B^{(\ell)^\top} \mathbf{W}_B^{(\ell-1)^\top} \mathbf{H}_A^{(\ell-1)} - 2 \mathbf{H}_A^{(\ell-1)^\top} \mathbf{P}^{(\ell-1)^\top} \mathbf{W}_B^{(\ell)^\top} \mathbf{W}_B^{(\ell-1)^\top} \right) \\
& \iff \arg \min_{\pi=\{\mathbf{P}^{(\ell)}\}} \sum_{\ell=1}^L \text{tr} \left(\mathbf{P}^{(\ell-1)^\top} \mathbf{W}_B^{(\ell)^\top} \mathbf{W}_B^{(\ell-1)^\top} \mathbf{H}_A^{(\ell-1)} \mathbf{H}_A^{(\ell-1)^\top} - 2 \mathbf{P}^{(\ell-1)^\top} \mathbf{W}_B^{(\ell)^\top} \mathbf{W}_B^{(\ell-1)^\top} \mathbf{H}_B^{(\ell-1)} \mathbf{H}_A^{(\ell-1)^\top} \right) \\
& \iff \arg \min_{\pi=\{\mathbf{P}^{(\ell)}\}} \sum_{\ell=1}^L \left(\text{tr} \left(\mathbf{P}^{(\ell-1)^\top} \mathbf{W}_B^{(\ell)^\top} \mathbf{W}_B^{(\ell-1)^\top} \mathbf{H}_A^{(\ell-1)} \mathbf{H}_A^{(\ell-1)^\top} \right) - 2 \text{tr} \left(\mathbf{P}^{(\ell-1)^\top} \mathbf{W}_B^{(\ell)^\top} \mathbf{W}_B^{(\ell-1)^\top} \mathbf{H}_B^{(\ell-1)} \mathbf{H}_A^{(\ell-1)^\top} \right) \right),
\end{aligned}$$

which also gives rise to Koopmans-Beckmann's QAPs.

For the last term, i.e.,

$$\begin{aligned}
& \arg \min_{\pi=\{\mathbf{P}^{(\ell)}\}} \sum_{\ell=1}^L \left\langle \mathbf{W}_A^{(\ell)} \mathbf{H}_A^{(\ell-1)} - \mathbf{W}_A^{(\ell)} \mathbf{P}^{(\ell-1)^\top} \mathbf{H}_B^{(\ell-1)}, \mathbf{P}^{(\ell)} \mathbf{W}_B^{(\ell)^\top} \mathbf{P}^{(\ell-1)^\top} \mathbf{H}_A^{(\ell-1)} - \mathbf{P}^{(\ell)} \mathbf{W}_B^{(\ell)^\top} \mathbf{H}_B^{(\ell-1)} \right\rangle_F \\
& \iff \arg \min_{\pi=\{\mathbf{P}^{(\ell)}\}} \sum_{\ell=1}^L \left\langle \left(\mathbf{W}_A^{(\ell)} \mathbf{H}_A^{(\ell-1)} - \mathbf{W}_A^{(\ell)} \mathbf{P}^{(\ell-1)^\top} \mathbf{H}_B^{(\ell-1)} \right) \left(\mathbf{W}_B^{(\ell)^\top} \mathbf{P}^{(\ell-1)^\top} \mathbf{H}_A^{(\ell-1)} - \mathbf{W}_B^{(\ell)^\top} \mathbf{H}_B^{(\ell-1)} \right)^\top, \mathbf{P}^{(\ell)} \right\rangle_F,
\end{aligned}$$

which entails solving bi-level matching problems.

Therefore, the objective can be rewritten as the summation of QAPs and bi-level matching problems and cannot be further simplified, which is NP-hard.

D More Experimental Details and Results

D.1 Detailed Experimental Settings

In this section, we introduce the detailed experimental setup. Before delving into details, recall that unless otherwise specified, in this paper we consider models trained on a training set, and then all the investigations are evaluated on a test set.

D.1.1 Spawning Method

Multi-Layer Perceptrons on the MNIST Dataset. In accordance with the settings outlined by Ainsworth et al. [1], we train multi-layer perceptron networks with three hidden layers, each consisting of 512 units, on the MNIST dataset. We adopt the ReLU activation between layers. Optimization is done with the Adam algorithm and a learning rate of 1.2×10^{-4} . The batch size is set to 60 and the total number of training epochs is 30. To find the modes that satisfy LMC, we start spawning from a common initialization $\theta^{(0)}$.

VGG-16 and ResNet-20 on the CIFAR-10 Dataset. In accordance with the settings outlined by Frankle et al. [8], We train the VGG-16 architecture [25] and the ResNet-20 architecture [11] on

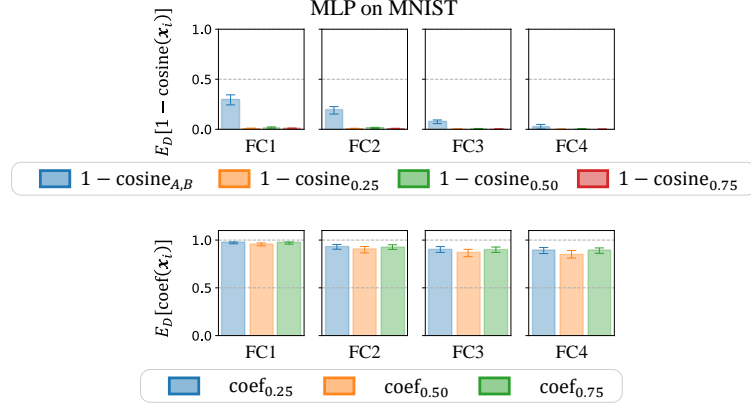


Figure 7: Comparison between $\mathbb{E}_{\mathcal{D}}[1 - \cosine_{\alpha}(\mathbf{x}_i)]$ and $\mathbb{E}_{\mathcal{D}}[1 - \cosine_{A,B}(\mathbf{x}_i)]$ and demonstration of $\mathbb{E}_{\mathcal{D}}[1 - \text{coef}_{\alpha}(\mathbf{x}_i)]$. The spawning method is used to obtain two linearly connected modes θ_A and θ_B . Results are presented for different layers of MLP on MNIST dataset, with $\alpha \in \{0.25, 0.5, 0.75\}$. Standard deviations across the dataset are reported by error bars.

the CIFAR-10 dataset. Data augmentation techniques include random horizontal flips and random 32×32 pixel crops. Optimization is done using SGD with momentum (momentum set to 0.9). A weight decay of 1×10^{-4} is applied. The learning rate is initialized at 0.1 and is dropped by 10 times at 80 and 120 epochs. The total number of epochs is 160. To find the modes that satisfy LMC, we start spawning after training 5 epochs for both VGG-16 and ResNet-20.

D.1.2 Permutation Method

For the permutation method, we follow the experimental settings of Ainsworth et al. [1] entirely, which are described below.

Multi-Layer Perceptrons on MNIST and CIFAR-10. Similar to the spawning method, we use multi-layer perceptron (MLP) networks with three hidden layers, each consisting of 512 units. For both MNIST and CIFAR-10, Optimization is performed using Adam with a learning rate of 1×10^{-3} . Both activation matching and weight matching are used to identify modes that satisfy LMC.

ResNet-20 on CIFAR-10. To achieve LMC, we modify the ResNet-20 architecture by incorporating LayerNorms in place of BatchNorms. Furthermore, we increase the width of ResNet-20 by a factor of 32. Data augmentation techniques include random horizontal flips, random 32×32 pixel crops, random resizes of the image between $0.8 \times$ and $1.2 \times$, and random rotations between $\pm 30^\circ$. The optimization process involves using SGD with momentum (set to 0.9). A weight decay regularization term of 5×10^{-4} is applied. A single cosine decay schedule with a linear warm-up is applied, where the learning rate is initialized to 1×10^{-6} and gradually increased to 0.1 over the course of an epoch, and then a single cosine decay schedule is applied for the remaining training. Only weight matching is used to identify modes that satisfy LMC.

Unlike the spawning method, VGG models are not used in the permutation method due to their inability to achieve LMC. Additionally, Ainsworth et al. [1] open-sourced their source code and pre-trained checkpoints. Therefore, we directly use the pre-trained checkpoints provided by Ainsworth et al. [1].

D.2 Verification of LLFC Co-Occurring with LMC

In this section, we provide extensive experimental results to verify that LLFC consistently co-occurs with LMC, and conduct a new experiment to demonstrate that the constant c is close to 1 in most cases. Both the spawning method and the permutation method are utilized to obtain linearly connected modes θ_A and θ_B . As shown in Figures 7 to 12, we include experimental results for MLP on the MNIST dataset (spawning method, activation matching, and weight matching), VGG-16 on the CIFAR-10 dataset (spawning method), ResNet-20 on the CIFAR-10 dataset (spawning method and weight matching) and MLP on the CIFAR-10 dataset (both activation matching and weight matching).

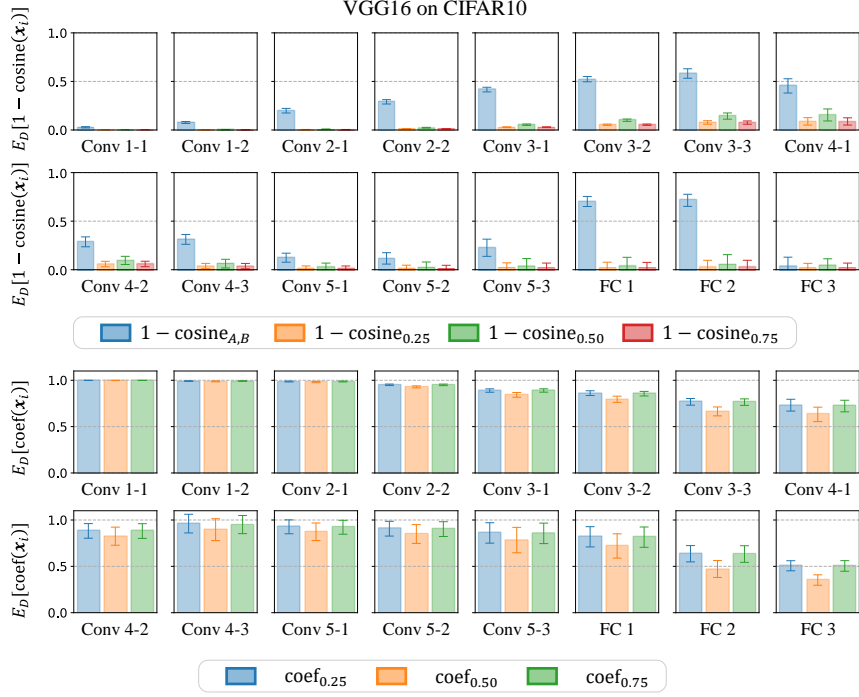


Figure 8: Comparison between $\mathbb{E}_{\mathcal{D}}[1 - \cosine_{\alpha}(\mathbf{x}_i)]$ and $\mathbb{E}_{\mathcal{D}}[1 - \cosine_{A,B}(\mathbf{x}_i)]$ and demonstration of $\mathbb{E}_{\mathcal{D}}[1 - \text{coef}_{\alpha}(\mathbf{x}_i)]$. The spawning method is used to obtain two linearly connected modes θ_A and θ_B . Results are presented for different layers of VGG-16 on the CIFAR-10 dataset, with $\alpha \in \{0.25, 0.5, 0.75\}$. Standard deviations across the dataset are reported by error bars.

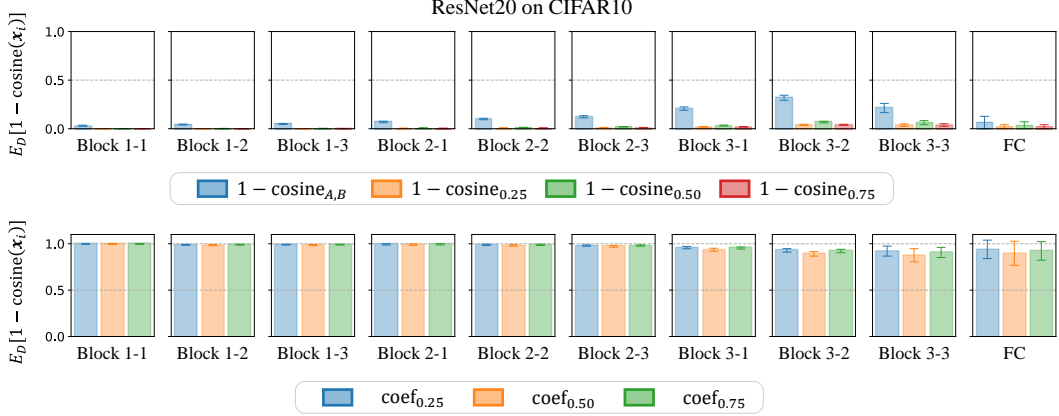


Figure 9: Comparison between $\mathbb{E}_{\mathcal{D}}[1 - \cosine_{\alpha}(\mathbf{x}_i)]$ and $\mathbb{E}_{\mathcal{D}}[1 - \cosine_{A,B}(\mathbf{x}_i)]$ and demonstration of $\mathbb{E}_{\mathcal{D}}[1 - \text{coef}_{\alpha}(\mathbf{x}_i)]$. The spawning method is used to obtain two linearly connected modes θ_A and θ_B . Results are presented for different layers of ResNet-20 on the CIFAR-10 dataset, with $\alpha \in \{0.25, 0.5, 0.75\}$. Standard deviations across the dataset are reported by error bars.

To verify the LLFC property on each data point \mathbf{x}_i in the test set \mathcal{D} , we measure $\cosine_{\alpha}(\mathbf{x}_i) = \cos[f^{(\ell)}(\alpha\theta_A + (1 - \alpha)\theta_B; \mathbf{x}_i), \alpha f^{(\ell)}(\theta_A; \mathbf{x}_i) + (1 - \alpha)f^{(\ell)}(\theta_B; \mathbf{x}_i)]$. We compare this to the baseline cosine similarity $\cosine_{A,B}(\mathbf{x}_i) = \cos[f^{(\ell)}(\theta_A; \mathbf{x}_i), f^{(\ell)}(\theta_B; \mathbf{x}_i)]$. In Figures 7 to 12, we conclude that the values of $\mathbb{E}_{\mathcal{D}}[1 - \cosine_{\alpha}(\mathbf{x}_i)]$ are close to 0 compared with $\mathbb{E}_{\mathcal{D}}[1 - \cosine_{A,B}(\mathbf{x}_i)]$, and thus verify our claim.

To show that the constant c is close to 1 in most cases, for each data point \mathbf{x}_i in the test set \mathcal{D} , we measure $\text{coef}_{\alpha}(\mathbf{x}_i) = \|f^{(\ell)}(\alpha\theta_A + (1 - \alpha)\theta_B; \mathbf{x}_i)\| \cosine_{\alpha}(\mathbf{x}_i) / \|\alpha f^{(\ell)}(\theta_A; \mathbf{x}_i) + (1 - \alpha)f^{(\ell)}(\theta_B; \mathbf{x}_i)\|$.

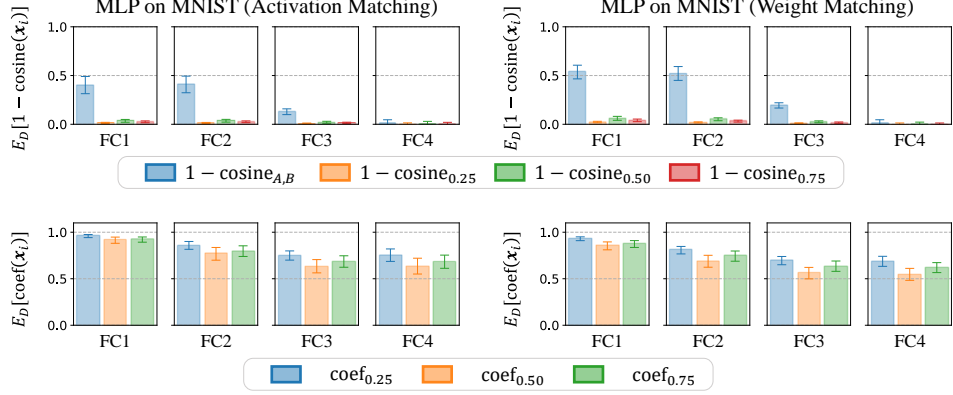


Figure 10: Comparison between $\mathbb{E}_D[1 - \cosine_\alpha(\mathbf{x}_i)]$ and $\mathbb{E}_D[1 - \cosine_{A,B}(\mathbf{x}_i)]$ and demonstration of $\mathbb{E}_D[1 - \text{coef}_\alpha(\mathbf{x}_i)]$. The activation matching and the weight matching are used to obtain two linearly connected modes θ_A and θ_B . Results are presented for different layers of MLP on the MNIST dataset, with $\alpha \in \{0.25, 0.5, 0.75\}$. Standard deviations across the dataset are reported by error bars.

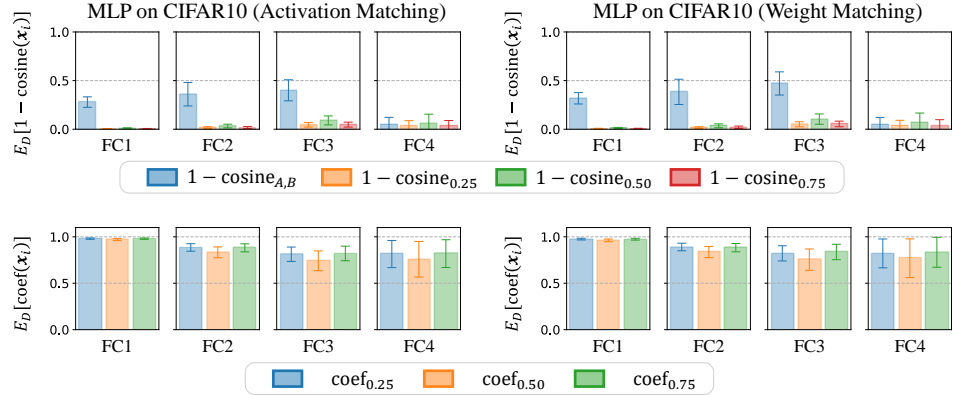


Figure 11: Comparison between $\mathbb{E}_D[1 - \cosine_\alpha(\mathbf{x}_i)]$ and $\mathbb{E}_D[1 - \cosine_{A,B}(\mathbf{x}_i)]$ and demonstration of $\mathbb{E}_D[1 - \text{coef}_\alpha(\mathbf{x}_i)]$. The activation matching and the weight matching are used to obtain two linearly connected modes θ_A and θ_B . Results are presented for different layers of MLP on the CIFAR-10 dataset, with $\alpha \in \{0.25, 0.5, 0.75\}$. Standard deviations across the dataset are reported by error bars.

$\alpha) f^{(\ell)}(\theta_B; \mathbf{x}_i)]\|$, where $\|f^{(\ell)}(\alpha\theta_A + (1-\alpha)\theta_B; \mathbf{x}_i)\| \cosine_\alpha(\mathbf{x}_i)$ denotes the length of $f^{(\ell)}(\alpha\theta_A + (1-\alpha)\theta_B; \mathbf{x}_i)$ projected on $\alpha f^{(\ell)}(\theta_A; \mathbf{x}_i) + (1-\alpha) f^{(\ell)}(\theta_B; \mathbf{x}_i)$. In Figures 7 to 12, we conclude that the values of $\mathbb{E}_D[\text{coef}_\alpha(\mathbf{x}_i)]$ are close to 1 in most cases, and thus verify our claim.

D.3 Verification of Weak Additivity for ReLU Activations

In this section, we provide experimental results on modes that satisfy LMC/LLFC found by permutation methods to verify that the condition of weak additivity for ReLU activations generally holds for modes that satisfy LMC/LLFC as well as the sparsity of the pre-activations. As shown in Figures 13 to 15, we include experimental results for MLP on the MNIST dataset (both activation matching and weight matching), MLP on the CIFAR-10 dataset (both activation matching and weight matching) and ResNet-20 on the CIFAR-10 dataset (weight matching).

To verify the condition of weak additivity for ReLU activations generally holds, on each data point \mathbf{x}_i in the test set \mathcal{D} , we compute $\text{Dist}_\sigma(\tilde{\mathbf{h}}_{i,A}, \tilde{\mathbf{h}}_{i,B}) = \text{dist}(\sigma(\tilde{\mathbf{h}}_{i,A} + \tilde{\mathbf{h}}_{i,B}), \sigma(\tilde{\mathbf{h}}_{i,A}) + \sigma(\tilde{\mathbf{h}}_{i,B}))$, where $\text{dist}(\mathbf{x}, \mathbf{y}) := \|\mathbf{x} - \mathbf{y}\|^2 / (\|\mathbf{x}\| \cdot \|\mathbf{y}\|)$. We compare $\text{Dist}_\sigma(\tilde{\mathbf{h}}_{i,A}, \tilde{\mathbf{h}}_{i,B})$ with $\text{Dist}_\sigma(\mathbf{r}_1, \mathbf{r}_2)$ where \mathbf{r}_1 and \mathbf{r}_2 are independent d_ℓ -dimensional random vectors sampled from $\mathcal{N}(\mathbf{0}, \mathbf{I})$. In Figures 13 to 15, we conclude that the values of $\text{Dist}_\sigma(\tilde{\mathbf{h}}_{i,A}, \tilde{\mathbf{h}}_{i,B})$ are generally small in comparison

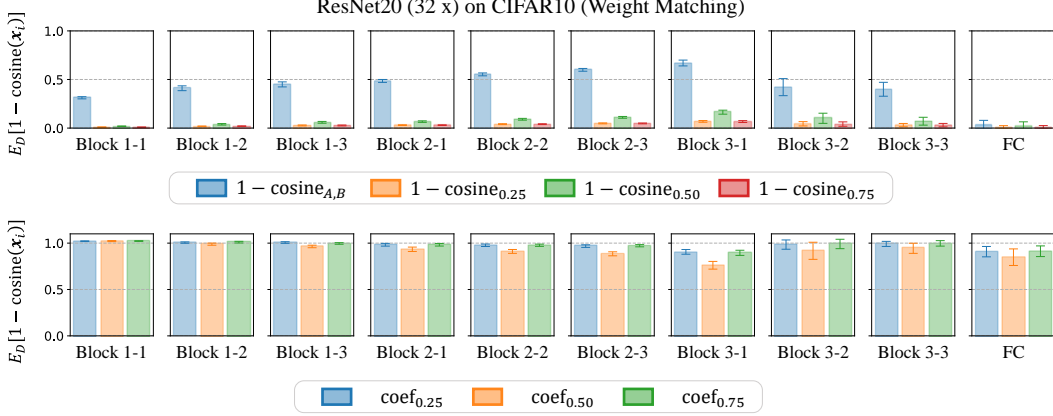


Figure 12: Comparison between $\mathbb{E}_D[1 - \cosine_\alpha(\mathbf{x}_i)]$ and $\mathbb{E}_D[1 - \cosine_{A,B}(\mathbf{x}_i)]$ and demonstration of $\mathbb{E}_D[1 - \text{coef}_\alpha(\mathbf{x}_i)]$. The weight matching is used to obtain two linearly connected modes θ_A and θ_B . Results are presented for different layers of ResNet-20 (32x) on the CIFAR-10 dataset, with $\alpha \in \{0.25, 0.5, 0.75\}$. Standard deviations across the dataset are reported by error bars.

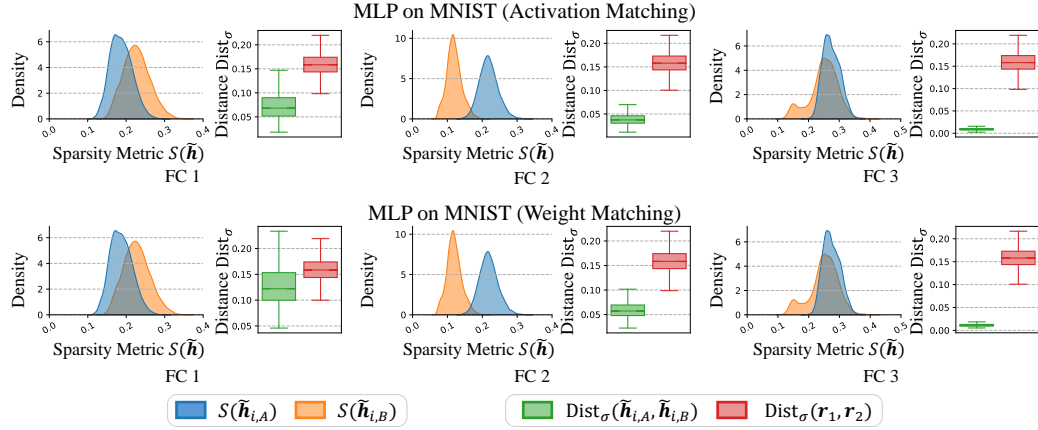


Figure 13: Distribution of the sparsity metrics $S(\tilde{\mathbf{h}}_{i,A})$, $S(\tilde{\mathbf{h}}_{i,B})$ over the test set and comparison between the distribution of the normalized distance $\text{Dist}_\sigma(\tilde{\mathbf{h}}_{i,A}, \tilde{\mathbf{h}}_{i,B})$ and $\text{Dist}_\sigma(\mathbf{r}_1, \mathbf{r}_2)$. Both the activation matching and the weight matching are used to obtain two modes that satisfy LLFC, θ_A and θ_B . Results are presented for different layers of MLP on the MNIST dataset. Notably, the sparsity metric has been revised.

to $\text{Dist}_\sigma(\mathbf{r}_1, \mathbf{r}_2)$. However, Figure 15 reveals that certain instances of $\text{Dist}_\sigma(\tilde{\mathbf{h}}_{i,A}, \tilde{\mathbf{h}}_{i,B})$ surpass $\text{Dist}_\sigma(\mathbf{r}_1, \mathbf{r}_2)$, indicating the weak additivity for ReLU activations is not perfectly satisfied in real scenarios. In fact, it is worth noting that the vector \mathbf{r} , which is sampled from a standard normal distribution, exhibits sparsity and approximately satisfies the weak additivity for ReLU activations. Hence, we can still conclude that the weak additivity condition generally holds for modes that satisfy LMC/LLFC.

To verify the sparsity claim, we leverage a sparsity metric, i.e., $S(\mathbf{x}) = \frac{\|\mathbf{x}\|_1}{n\|\mathbf{x}\|_\infty}$ ($\mathbf{x} \in \mathbb{R}^n$) (The average absolute value of each entry in the vector dividing by the maximum absolute value among the entries). We measure the sparsity of the pre-activations using this metric, denoted as $S(\tilde{\mathbf{h}}_{i,A})$ and $S(\tilde{\mathbf{h}}_{i,B})$, respectively. In Figures 13 to 15, the values of $S(\tilde{\mathbf{h}}_{i,A})$ and $S(\tilde{\mathbf{h}}_{i,B})$ are small, thus providing further supports for the sparsity claim.

Additionally, both activation matching and weight matching do not have the capability to alter the sparsity of the pre-activations. Hence, as depicted in Figures 13 and 14, the sparsity results

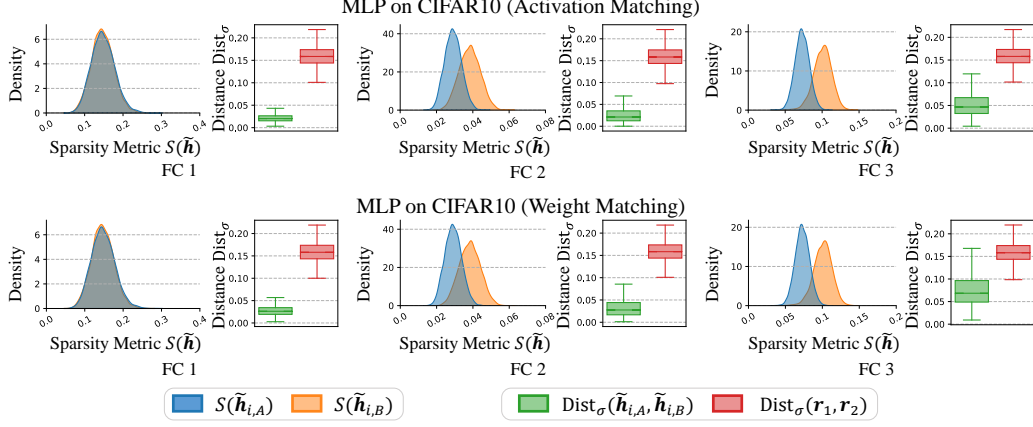


Figure 14: Distribution of the sparsity metrics $S(\tilde{h}_{i,A})$, $S(\tilde{h}_{i,B})$ over the test set and comparison between the distribution of the normalized distance $\text{Dist}_\sigma(\tilde{h}_{i,A}, \tilde{h}_{i,B})$ and $\text{Dist}_\sigma(r_1, r_2)$. Both the activation matching and the weight matching are used to obtain two modes that satisfy LLFC, θ_A and θ_B . Results are presented for different layers of MLP on the CIFAR-10 dataset. Notably, the sparsity metric has been revised.

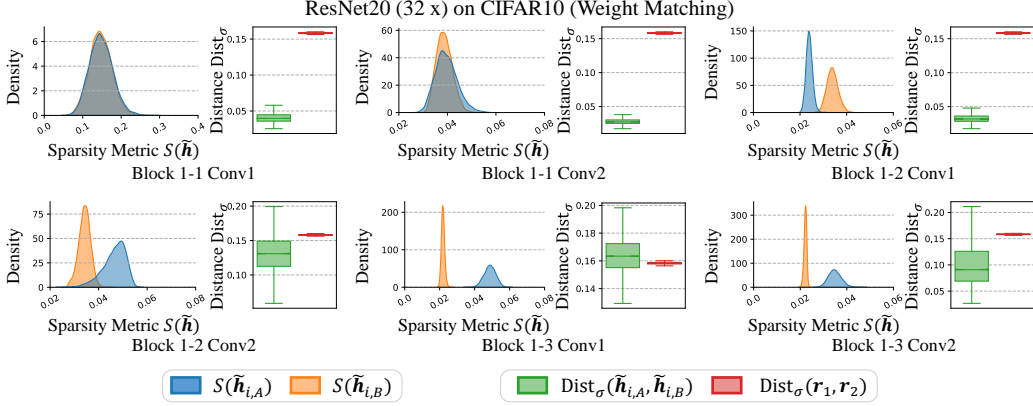


Figure 15: Distribution of the sparsity metrics $S(\tilde{h}_{i,A})$, $S(\tilde{h}_{i,B})$ over the test set and comparison between the distribution of the normalized distance $\text{Dist}_\sigma(\tilde{h}_{i,A}, \tilde{h}_{i,B})$ and $\text{Dist}_\sigma(r_1, r_2)$. The weight matching is used to obtain two modes that satisfy LLFC, θ_A and θ_B . Results are presented for different layers of ResNet-20 (32x) on the CIFAR-10 dataset. Notably, the sparsity metric has been revised.

remain consistent for a given layer, regardless of whether activation matching or weight matching is employed.

D.4 Verification of Commutativity

In this section, we provide more experimental results on various datasets and model architectures to verify the commutativity property for modes that satisfy LLFC. As shown in Figures 16 to 18, we include more experiments results for VGG-16 on the CIFAR-10 dataset (spawning method), MLP on the MNIST dataset (activation matching) and MLP on the CIFAR-10 dataset (both activation matching and weight matching).

To verify the commutativity generally holds for modes that satisfy LLFC, for test set \mathcal{D} , we compute $\text{Dist}_{com} = \text{dist} \left(\text{vec}(\mathbf{W}_A^{(\ell)} \mathbf{H}_A^{(\ell-1)} + \mathbf{W}_B^{(\ell)} \mathbf{H}_B^{(\ell-1)}), \text{vec}(\mathbf{W}_A^{(\ell)} \mathbf{H}_B^{(\ell-1)} + \mathbf{W}_B^{(\ell)} \mathbf{H}_A^{(\ell-1)}) \right)$ ⁵. Fur-

⁵We also conduct experiments on CNNs. For a Conv layer, the forward propagation will be denoted as $\mathbf{W}\mathbf{H}$ similar to a linear layer.

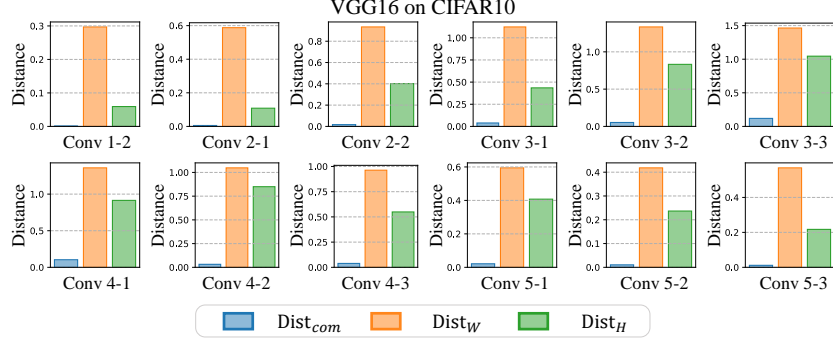


Figure 16: Comparison of Dist_{com} , Dist_W , and Dist_H . The spawning method is used to obtain two modes that satisfy LLFC, θ_A and θ_B . The results are presented for different layers of VGG-16 on the CIFAR-10 dataset.

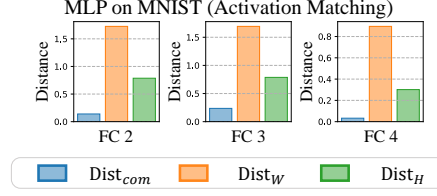


Figure 17: Comparison of Dist_{com} , Dist_W , and Dist_H . The activation matching is used to obtain two modes that satisfy LLFC, θ_A and θ_B . The results are presented for different layers of MLP on the MNIST dataset.

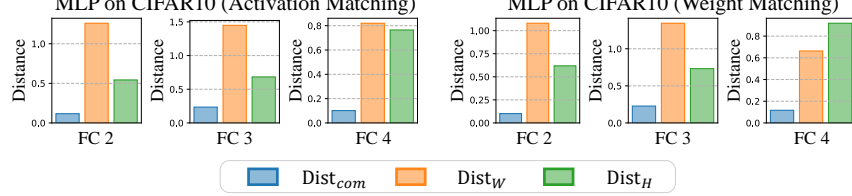


Figure 18: Comparison of Dist_{com} , Dist_W , and Dist_H . Both the activation matching and weight matching are used to obtain two modes that satisfy LLFC, θ_A and θ_B . The results are presented for different layers of MLP on the CIFAR10 dataset.

Layer ℓ	FC 1	FC 2	FC 3
$\text{Err}_{\mathcal{D}(B > \ell \circ A \leq \ell)}$	2.69	2.11	1.92

Table 1: Error rates (%) of stitched MLP on the MNIST test set. The model stitching is employed in different layers. The spawning method is used to obtain two neural networks that satisfy LLFC, i.e., A and B . Error rates (%) of A and B are 1.9 and 1.77, respectively.

thermore, we compare Dist_{com} with $\text{Dist}_W = \text{dist}(\text{vec}(\mathbf{W}_A^{(\ell)}), \text{vec}(\mathbf{W}_B^{(\ell)}))$ and $\text{Dist}_H = \text{dist}(\text{vec}(\mathbf{H}_A^{(\ell-1)}), \text{vec}(\mathbf{H}_B^{(\ell-1)}))$, respectively. In Figures 16 to 18, Dist_{com} is negligible compared with Dist_W and Dist_H , confirming the commutativity condition.

Notably, the experiments are not conducted on the first Conv/Linear layer of the model because the commutativity condition is naturally satisfied for the first layer where $\mathbf{H}_A^{(0)} = \mathbf{H}_B^{(0)} = \mathbf{X}$ where \mathbf{X} is the input data matrix.

Layer ℓ	Conv 1-1	Conv 1-2	Conv 2-1	Conv 2-2	Conv 3-1
$\text{Err}_{\mathcal{D}(B_{>\ell} \circ A_{\leq \ell})}$	7.2	8.43	8.39	9.91	11.84
Layer ℓ	Conv 3-2	Conv 3-3	Conv 4-1	Conv 4-2	Conv 4-3
$\text{Err}_{\mathcal{D}(B_{>\ell} \circ A_{\leq \ell})}$	9.55	8.22	7.61	6.99	7.05
Layer ℓ	Conv 5-1	Conv 5-2	Conv 5-3	FC 1	FC 2
$\text{Err}_{\mathcal{D}(B_{>\ell} \circ A_{\leq \ell})}$	6.91	6.88	6.88	7.07	6.92

Table 2: Error rates (%) of stitched VGG-16 on the CIFAR-10 test set. The model stitching is employed in different layers. The spawning method is used to obtain two neural networks that satisfy LLFC, i.e., A and B . Error rates (%) of A and B are 6.87 and 7.1, respectively.

Layer ℓ	Block 1-1	Block 1-2	Block 1-3	Block 2-1	Block 2-2	Block 2-3	Block 3-1	Block 3-2	Block 3-3
$\text{Err}_{\mathcal{D}(B_{>\ell} \circ A_{\leq \ell})}$	10.88	10.57	13.35	10.64	10.74	10.55	12.27	11.8	8.99

Table 3: Error rates (%) of stitched ResNet-20 on the CIFAR-10 test set. The model stitching is employed in different layers. The spawning method is used to obtain two neural networks that satisfy LLFC, i.e., A and B . Error rates (%) of A and B are 8.69 and 8.58, respectively.

D.5 Experiments on Model Stitching

Model stitching [17, 3] is commonly employed to analyze neural networks’ internal representations. Let A and B represent neural networks with identical architectures. Given a loss function \mathcal{L} , model stitching involves finding a stitching layer s (e.g., a linear 1×1 convolutional layer) such that the minimization of $\mathcal{L}(B_{>\ell} \circ s \circ A_{\leq \ell})$ is achieved. Here, $B_{>\ell}$ denotes the mapping from the activations of the ℓ -th layer of network B to the final output, $A_{\leq \ell}$ denotes the mapping from the input to the activations of the ℓ -th layer of network A , and \circ represents function composition.

In this section, we explore a stronger form of model stitching. Specifically, given two neural networks A and B that satisfy LLFC, we evaluate the accuracy of $B_{>\ell} \circ A_{\leq \ell}$ over the test set \mathcal{D} without finding a stitching layer, i.e., $\text{Err}_{\mathcal{D}(B_{>\ell} \circ A_{\leq \ell})}$. As shown in Tables 1 to 3, we include experimental results for MLP on the MNIST dataset, VGG-16 on CIFAR-10 the dataset and ResNet-20 on the CIFAR-10 dataset. Only the spawning method is utilized to find modes that satisfy LLFC. The results depicted in Tables 1 to 3 demonstrate that the error rates of the stitched model on the test set closely resemble the error rates of the original models A and B , regardless of the dataset or model architecture. This observation suggests that models that satisfy LLFC encode similar information, which can be decoded across different models. Subsequently, the experiments of model stitching provides new insights towards the commutativity property, i.e., $\forall \ell \in [L], \mathbf{W}_B^{(\ell)} \mathbf{H}_A^{(\ell-1)} \approx \mathbf{W}_B^{(\ell)} \mathbf{H}_B^{(\ell-1)}$.

D.6 Verification of Similar Principal Directions of Model Weights

In this section, we provide more experimental results on various datasets and model architectures to verify that the modes found by the spawning method share similar principal directions of model weights in each layer. As shown in Figures 19 and 20, we include the experimental results for ResNet-20 on the CIFAR-10 dataset and additional layers of VGG-16 on the CIFAR-10 dataset.

To verify our claim, specifically, given the model weights $\mathbf{W}_A^{(\ell)}$ ⁶ and $\mathbf{W}_B^{(\ell)}$ of two modes θ_A and θ_B at ℓ -th layer, we compute the minimal principal angle $\beta^{(\ell)}$ between the subspaces spanned by top- k singular vectors of $\mathbf{W}_A^{(\ell)}$ and $\mathbf{W}_B^{(\ell)}$, respectively. We compare the value of $1 - \cos \beta_{LMC}$ of two modes satisfying LMC to $1 - \cos \beta_{not \ LMC}$ of two modes that are independently trained (not satisfying LMC). In Figures 19 and 20, we observe that the angle β_{LMC} is close to zero compared with $\beta_{not \ LMC}$. Therefore, Figures 19 and 20 offer additional evidence supporting the claim that the modes obtained through the spawning method exhibit similar principal directions in their model weights.

⁶Typically, the weight \mathbf{W} for a Conv layer has shape (# of output channels, # of input channels, height, width) and we reshape \mathbf{W} to a matrix with dimensions (# of output channels, # of input channels \times height \times width). The same method is applied in later sections.

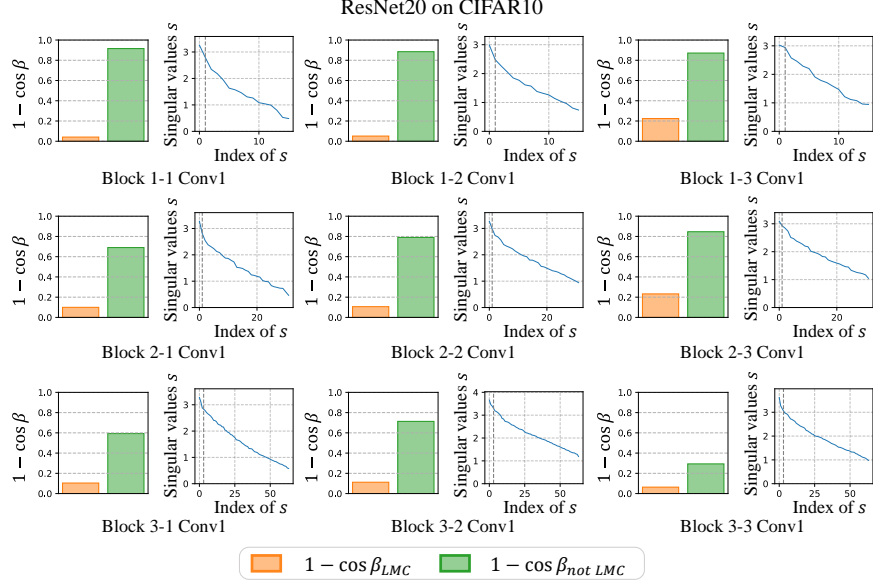


Figure 19: Comparison of $1 - \cos \beta_{LMC}$ and $1 - \cos \beta_{not LMC}$ and singular values of weight matrix of layers of θ_A in a descending order. The grey dashed line marked the value of k chosen for each β . The spawning method is used to obtain two modes that satisfy LLFC, θ_A and θ_B . The results are presented for different layers of ResNet-20 on the CIFAR-10 dataset.

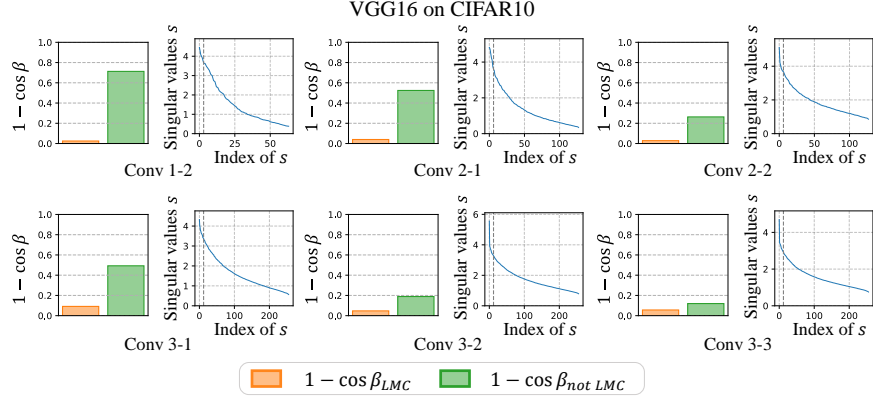


Figure 20: Comparison of $1 - \cos \beta_{LMC}$ and $1 - \cos \beta_{not LMC}$ and singular values of weight matrix of layers of θ_A in a descending order. The grey dashed line marked the value of k chosen for each β . The spawning method is used to obtain two modes that satisfy LLFC, θ_A and θ_B . The results are presented for different layers of VGG-16 on the CIFAR-10 dataset.

E Discussion on Git Re-basin [1]

In this section, we investigate the ability of permutation methods to achieve LMC. While we have interpreted the activation matching and weight matching methods proposed by Ainsworth et al. [1] as guaranteeing the commutativity property, we have yet to address why permutation methods can ensure the satisfaction of this property. Thus, in order to delve into the capability of permutation methods, we must address the question of why these methods are capable of ensuring the satisfaction of the commutativity property.

Low-rank model weights and activations contribute to ensure the commutativity property. We now consider a stronger form of the commutativity property, where given two modes θ_A and θ_B and a dataset \mathcal{D} , we have:

$$\forall \ell \in [L], \mathbf{W}_A^{(\ell)} \mathbf{H}_A^{(\ell-1)} = \mathbf{W}_A^{(\ell)} \mathbf{H}_B^{(\ell-1)} \wedge \mathbf{W}_B^{(\ell)} \mathbf{H}_B^{(\ell-1)} = \mathbf{W}_B^{(\ell)} \mathbf{H}_A^{(\ell-1)}.$$

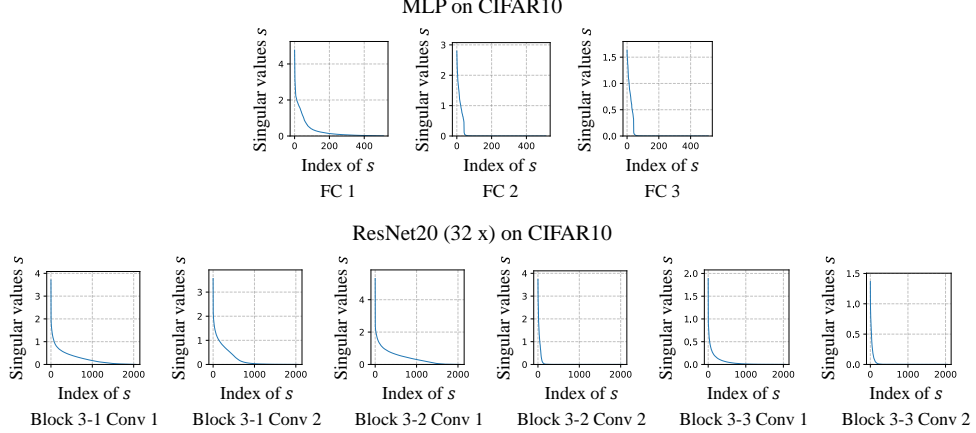


Figure 21: Singular values of weight matrix $\mathbf{W}^{(\ell)}$ of ℓ -th layer of θ in a descending order. Here, θ can be used to achieve LMC with weight matching. The results are presented for different layers of various model architectures and datasets.

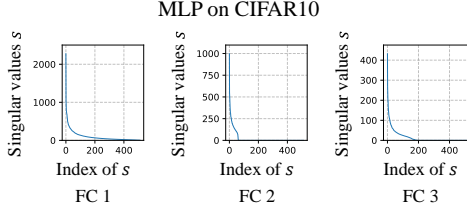


Figure 22: Singular values of post-activations $\mathbf{H}^{(\ell)}$ of ℓ -th layer of θ over the whole test set \mathcal{D} in a descending order. Here, θ can be used to achieve LMC with activation matching. The results are presented for different layers of MLP on the CIFAR-10 dataset.

Thus, to satisfy the commutativity property for a given layer ℓ , we can employ the permutation method to find a permutation matrix $\mathbf{P}^{(\ell-1)}$ such that:

$$\mathbf{W}_A^{(\ell)} \left(\mathbf{H}_A^{(\ell-1)} - \mathbf{P}^{(\ell-1)} \mathbf{H}_B^{(\ell-1)} \right) = 0 \wedge \mathbf{P}^{(\ell)} \mathbf{W}_B^{(\ell)} \left(\mathbf{H}_B^{(\ell-1)} - \mathbf{P}^{(\ell-1)^\top} \mathbf{H}_A^{(\ell-1)} \right) = 0.$$

In a homogeneous linear system $\mathbf{W}\mathbf{X} = 0$, a low-rank matrix \mathbf{W} allows for a larger solution space for \mathbf{X} . Therefore, if the ranks of $\mathbf{W}_A^{(\ell)}$ and $\mathbf{W}_B^{(\ell)}$ are low, it becomes easier to find a permutation matrix $\mathbf{P}^{(\ell-1)}$ that satisfies the commutativity property. Similarly, if we consider another form of commutativity property:

$$\forall \ell \in [L], \mathbf{W}_A^{(\ell)} \mathbf{H}_A^{(\ell-1)} = \mathbf{W}_B^{(\ell)} \mathbf{H}_A^{(\ell-1)} \wedge \mathbf{W}_B^{(\ell)} \mathbf{H}_B^{(\ell-1)} = \mathbf{W}_A^{(\ell)} \mathbf{H}_B^{(\ell-1)}.$$

Then, to ensure the commutativity property, we need to find $\mathbf{P}^{(\ell-1)}$ and $\mathbf{P}^{(\ell)}$ such that

$$\left(\mathbf{W}_A^{(\ell)} - \mathbf{P}^{(\ell)} \mathbf{W}_B^{(\ell)} \mathbf{P}^{(\ell-1)^\top} \right) \mathbf{H}_A^{(\ell-1)} = 0 \wedge \left(\mathbf{P}^{(\ell)} \mathbf{W}_B^{(\ell)} \mathbf{P}^{(\ell-1)^\top} - \mathbf{W}_A^{(\ell)} \right) \mathbf{P}^{(\ell-1)} \mathbf{H}_B^{(\ell-1)} = 0.$$

Then, if the ranks of $\mathbf{H}_A^{(\ell-1)}$ and $\mathbf{H}_B^{(\ell-1)}$ are low, it is easier to find the permutation matrices to satisfy the condition. In real scenarios, both model weights (see Figure 21) and activations (see Figure 22) are approximately low-rank, which helps the permutation methods satisfy the commutativity property.

Additionally, Ainsworth et al. [1] mentioned two instances where permutation methods can fail: models with insufficient width and models in the early stages of training. In both cases, the model weights often fail to satisfy the low-rank model weight condition. In the first scenario, when the model lacks sufficient width, meaning that the dimension of the weight matrix approaches the rank of the weight matrix, the low-rank condition may not be met. For example, compared the singular values of ResNet-20 (32x) (see Figure 21) with singular values of ResNet-20 (1x) (see Figure 19), it is evident that in the wider architecture, the proportion of salient singular values is smaller. In the

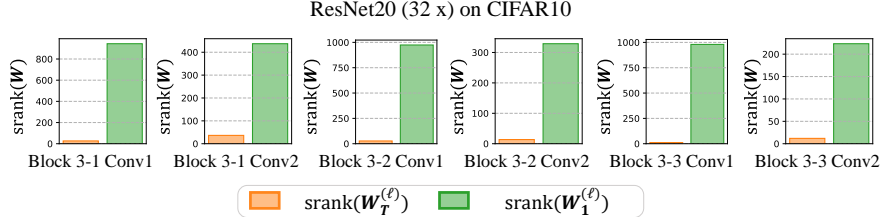


Figure 23: Comparison between the stable rank $\text{srank}(\mathbf{W}_T^{(\ell)})$ and $\text{srank}(\mathbf{W}_1^{(\ell)})$. Here, $\mathbf{W}_T^{(\ell)}$ denotes the weight matrix of the ℓ -th layer of the model θ_T in the terminal phase of training. Similarly, $\mathbf{W}_1^{(\ell)}$ denotes the weight matrix of the ℓ -th layer of the model θ_1 in the early stage of training (1 epoch indeed). Also, the stable rank can be calculated as $\text{srank}(\mathbf{W}) = \frac{\|\mathbf{W}\|_F^2}{\|\mathbf{W}\|_2^2}$. The results are presented for different layers of ResNet-20 (32x) on the CIFAR-10 dataset.

second scenario, during the initial stages of training, the weight matrices resemble random matrices and may not exhibit low-rank characteristics. For example, as shown in Figure 23, the stable ranks of weight matrices of the model after convergence are significantly smaller than those of the model in the early stage of training. Consequently, permutation methods may struggle to find suitable permutations that fulfill the commutativity property, resulting in the inability to obtain modes that satisfy LMC.